

Spectral analysis of the barium central star of the planetary nebula Hen 2–39[★]

L. Löbbling^{1,2}, H. M. J. Boffin¹, and D. Jones^{3,4}

¹ European Southern Observatory, Karl-Schwarzschild-Str. 2, D-85748 Garching bei München, Germany

² Institute for Astronomy and Astrophysics, Kepler Center for Astro and Particle Physics, Eberhard Karls University, Sand 1, D-72076 Tübingen, Germany
e-mail: loebbling@astro.uni-tuebingen.de

³ Instituto de Astrofísica de Canarias, E-38205 La Laguna, Tenerife, Spain

⁴ Departamento de Astrofísica, Universidad de La Laguna, E-38206 La Laguna, Tenerife, Spain

Received 19 October 2018; accepted 6 February 2019

ABSTRACT

Context. Barium stars are peculiar red giants characterized by an overabundance of the elements synthesized in the slow neutron-capture nucleosynthesis (s-process elements) along with an enrichment in carbon. These stars are discovered in binaries with white dwarf companions. The more recently formed of these stars are still surrounded by a planetary nebula.

Aims. Precise abundance determinations of the various s-process elements, of further key elements that act as indicators for effectiveness of nucleosynthesis on the asymptotic giant branch and, especially, of the lightest, short-lived radionuclide technetium will establish constraints for the formation of s-process elements in asymptotic giant branch stars as well as mass transfer through, for example, stellar wind, Roche-lobe overflow, and common-envelope evolution.

Methods. We performed a detailed spectral analysis of the K-type subgiant central star of the planetary nebula Hen 2–39 based on high-resolution optical spectra obtained with the Ultraviolet and Visual Echelle Spectrograph at the Very Large Telescope using local thermodynamic equilibrium model atmospheres.

Results. We confirm the effective temperature of $T_{\text{eff}} = (4350 \pm 150)$ K for the central star of the planetary nebula Hen 2–39. It has a photospheric carbon enrichment of $[C/H] = 0.36 \pm 0.08$ and a barium overabundance of $[Ba/Fe] = 1.8 \pm 0.5$. We find a deficiency for most of the iron-group elements (calcium to iron) and establish an upper abundance limit for technetium ($\log \epsilon_{\text{Tc}} < 2.5$).

Conclusions. The quality of the available optical spectra is not sufficient to measure abundances of all s-process elements accurately. Despite large uncertainties on the abundances as well as on the model yields, the derived abundances are most consistent with a progenitor mass in the range $1.75\text{--}3.00 M_{\odot}$ and a metallicity of $[Fe/H] = -0.3 \pm 1.0$. This result leads to the conclusion that the formation of such systems requires a relatively large mass transfer that is most easily obtained via wind-Roche lobe overflow.

Key words. planetary nebulae: individual: Hen 2–39 – Stars: abundances – Stars: evolution – Stars: AGB and post-AGB stars – Stars: chemically peculiar – Stars: binaries: general

1. Introduction

So far, only a small number of planetary nebulae (PNe) have been identified to host a binary with a giant or subgiant component dominating the optical wavelength range and showing peculiar surface element abundances that indicate late stage stellar evolution nuclear synthesis. These stars exhibit signatures of slow neutron-capture nucleosynthesis (s-process) in their spectra and in some cases an enrichment in carbon (C).

For the object of this work, the central star (CS) of the PN Hen 2–39 (PN G283.8–04.2, Wray 16–64; Henize 1967; Acker et al. 1992; Wray 1966), Miszalski et al. (2013b) determined an overabundance for the s-process element barium (Ba) of $[Ba/Fe]^1 = 1.5 \pm 0.25$ and an enrichment of $[C/H] = 0.42 \pm 0.02$ in a spectral analysis based on mid-resolution spectra obtained with the Southern African Telescope (SALT; Buckley et al. 2006) with the Robert Stobie Spectro-

graph (RSS; Burgh et al. 2003; Kobulnicky et al. 2003). These findings confirm the membership of the K-type nucleus of Hen 2–39 in the small group of Ba central stars of planetary nebulae (CSPNe) along with LoTr 5, WeBo 1, and Abell 70 (Thevenin & Jasniewicz 1997; Bond et al. 2003; Miszalski et al. 2012; Tyndall et al. 2013; Aller et al. 2018).

Ba CSPNe are prime examples of progenitors of Ba stars that were described by Bidelman & Keenan (1951). Because of their evolutionary status, namely still being on the main sequence or a red giant, these stars did not yet experience AGB nucleosynthesis and, thus, cannot have synthesized heavy elements. McClure et al. (1980) discovered the binary nature of Ba stars and proposed that mass transfer was key to explain these sources. Boffin & Jorissen (1988) performed detailed simulations of wind mass transfer to explain the pollution of the Ba star from an evolved companion with the products of asymptotic giant branch (AGB) nucleosynthesis that are dredged up to the stellar surface (Herwig 2005; Werner & Herwig 2006). More recently, other mechanisms were proposed in which the material is transferred to the still unevolved companion (Boffin 2015) via Roche-lobe overflow (RLOF; e.g., Han et al. 1995) or wind-

[★] Based on data products from observations made with ESO Telescopes at the La Silla Paranal Observatory under program ID 093.D-0332(A).

¹ $[A/B] = \log(n_A/n_B) - \log(n_{A,\odot}/n_{B,\odot})$ with the number fractions n for element A and B

RLOF (e.g., Nagrae et al. 2004; Mohamed & Podsiadlowski 2007; Abate et al. 2013).

This scenario is strongly supported by the fact that, so far, all Ba stars are found in binaries with white dwarf (WD) companions (McClure et al. 1980; McClure 1983; Jorissen & Mayor 1988; McClure & Woodsworth 1990; Jorissen et al. 1998), which is also definitely clear for the Ba CSPNe since the Ba star is not hot enough to ionize the ambient ejected material that is visible as the surrounding PN. Although the (pre-)WD companion must be there without any doubt, it can be difficult to detect against the bright companion even in the UV. Recently, more and more WD companions of Ba stars (Gray et al. 2011) and pre-WD companions of Ba CSPNe have been detected (e.g., Abell 70, Miszalski et al. 2012), which doubtlessly confirms the formation scenario. The still poorly understood mechanism of mass transfer in these systems is subject of ongoing research. The challenge is to determine their orbital parameters, such as eccentricity and period and to reproduce these with theoretical binary evolution models (Saladino et al. 2018; De Marco 2009).

These stars are expected to show orbital periods of several hundred days, which are typical values for Ba stars (Jorissen et al. 1998). However, there is the CSPN binary in the Necklace Nebula (PN G054.6–03.4; Corradi et al. 2011) standing out toward shorter periods. Miszalski et al. (2013a) found a period of 1.16 d for the post-CE system from the analysis of the C-dwarf secondary. On the other side of the period range, current analyses also indicate that there are systems with values up to several years and with larger eccentricities (Jones et al. 2017).

Ba CSPNe are ideal to study AGB nucleosynthesis. They provide a snapshot of an evolutionary stage with ideal conditions for analyzing not only the polluted cool (sub)giant star but also the ejected material of the nebula around the polluting post-AGB star (e.g., Madonna et al. 2017, 2018). The short duration of the PN phase ($\approx 10^4$ yrs) guarantees that the mass transfer happened recently and that the companion has not yet had time to adjust. Also, in some cases, the polluted star is still unevolved and did not experience the first dredge-up (DU) that would affect the surface element composition including the nucleosynthesis outcomes from the polluting post-AGB star.

By comparing the results of our comprehensive spectral analysis to theoretical AGB nucleosynthesis models (Karakas & Lugaro 2016; Karakas et al. 2018), new insights into Ba stars and PNe are gained. It is worth mentioning the s-process mechanisms including atomic reaction rates, the source of neutrons and neutron exposure, internal stellar structures, and mixing processes occurring in a thermal-pulsing AGB star. This allows us to constrain the progenitor mass of the post-AGB star and the number of thermal pulses (TPs) on the AGB. Including binary evolution models (Saladino et al. 2018; De Marco 2009), these objects offer the opportunity to study the CE process and (wind-)RLOF, which are still far from being understood (Miszalski et al. 2013a; Jones & Boffin 2017), and in addition the fraction of mass transferred (Boffin & Jorissen 1988) and, following from this, the dilution factor in the Ba star itself and, thus, the mixing processes at work in (sub)giant stars (Husti et al. 2009). In particular, Ba CSPNe such as Hen 2–39 offer the possibility to detect technetium (Tc), which is the lightest element with no stable isotopes, in their atmospheres. This element was first detected by Merrill (1952) in the atmospheres of red giants, which proved that it is synthesized in evolved stars, since the half-life of ^{99}Tc of 210 000 yrs² is much shorter

than the previous giant evolutionary phase. It is thus only observed in AGB stars currently undergoing thermal pulses (TPs; Van Eck & Jorissen 1999; Lebzelter & Hron 2003) and, hence, the determination of the Tc surface abundance of the Ba CSPN indicates the mass-transfer link between the binary components in the PN and establishes a definite indicator for the existence of the third dredge-up (TDU). Assuming a typical post-AGB age of some $10^3 - 10^4$ yrs (Miller Bertolami 2016) for the primary component and taking into account that the dynamical process of mass transfer is short compared to this number (Iben & Livio 1993; Chen et al. 2017), a large fraction of the transferred Tc should still be present in the stellar atmosphere.

We describe the observations, stellar atmosphere models, and analysis techniques in Sect. 2 and 3, respectively. The spectral analysis follows in Sects. 4 and 5. The results are discussed in Sect. 6. We summarize and conclude in Sect. 7.

2. Observations

The spectral analysis of Hen 2–39 is based on spectra in the optical wavelength range obtained with the Ultraviolet and Visual Echelle Spectrograph (UVES; Dekker et al. 2000) at the Very Large Telescope (VLT) at the Paranal Observatory of the European Southern Observatory under ESO program 093.D–0332(A). The data products created from this data were retrieved from the ESO Science Archive Facility. The observation log, including the signal-to-noise ratio (S/N), of the spectra used in this paper is shown in Tab. A.1. All spectra were taken with a resolving power of $R = 42\,000 - 44\,000$.

We used the spectral analysis code ISpec (Blanco-Cuaresma et al. 2014) to determine the radial velocities for each single observation via cross-correlation with a model template spectrum created using the fundamental parameters T_{eff} , $\log g$, C abundance, and metallicity determined by Miszalski et al. (2013b). The heliocentric corrected radial velocities for the 18 observations are given in Table 1. To improve the S/N, all observations were shifted to the rest-frame velocity and subsequently co-added. To simulate the resolution of the instrument, all synthetic spectra shown in this work were convolved with Gaussians (full width half maximum (FWHM) = 0.12 Å).

3. Model atmospheres, atomic data, and analysis techniques

We used the stellar synthesis code SPECTRUM³ (Gray & Corbally 1994, version 2.76) to calculate synthetic spectra for the analysis of the observed high-resolution spectra with the ATLAS9 model atmosphere grids⁴ (Kurucz 1991; Castelli & Kurucz 2003) as input. These one-dimensional models are based upon the solar abundances from Grevesse & Sauval (1998) and are calculated under the presumption of plane-parallel geometry and local thermodynamic equilibrium (LTE), which is valid for stars in this temperature and gravity regime (Hubeny et al. 2003). For the wavelength values and oscillator strengths of the lines selected in our analysis, we used the values provided within the distribution of SPECTRUM. Data for Tc I were retrieved from the Atomic Spectra Database⁵ of the National Institute of Standards and Technology (NIST). For Tc II, we used the data provided by Palmeri et al.

³ <http://www.appstate.edu/~grayro/spectrum/spectrum.html>

⁴ <http://kurucz.harvard.edu/grids.html>

⁵ <https://www.nist.gov/pml/atomic-spectra-database>

² Los Alamos National Laboratory Periodic Table <http://periodic.lanl.gov>

Table 1: Observation time and heliocentric radial velocities for the 18 observations of the Ba CSPN of Hen 2–39.

MJD	v_{rad}
56750.117	44.79 ± 1.06
56750.135	44.76 ± 1.01
56750.154	46.61 ± 1.00
56750.172	45.64 ± 1.09
56751.032	46.05 ± 0.93
56751.050	46.47 ± 0.92
56751.070	46.34 ± 1.07
56751.088	46.29 ± 1.03
56751.109	45.35 ± 1.05
56751.127	45.17 ± 1.05
56760.108	45.43 ± 0.94
56760.126	45.56 ± 1.06
56762.018	45.79 ± 1.09
56762.035	45.21 ± 1.00
56762.053	45.64 ± 1.06
56762.070	45.91 ± 1.08
56762.088	45.96 ± 1.10
56762.106	46.24 ± 1.09

(2007). We calculated an extensive grid of synthetic spectra spanning from $T_{\text{eff}} = 3500$ K to 6000 K ($\Delta T_{\text{eff}} = 250$ K between 4000 K and 5000 K and $\Delta T_{\text{eff}} = 500$ K otherwise) and from $\log(g/\text{cm/s}^2) = 0.0$ to 4.0 ($\Delta \log g = 0.5$) with a metallicity of $[M/H] = -0.3$ around the literature values of $T_{\text{eff}} = 4250 \pm 150$ K and $\log g = 2.0 \pm 0.5$ (Miszalski et al. 2013b). For the determination of abundances, we relied on the model with $T_{\text{eff}} = 4250$ K and $\log g = 2.5$ and varied the abundance of one single element over a range of at least 2.5 dex with a step of 0.5 dex. The exceptions to this are C, for which we varied the abundance in steps of 0.05 dex over a range of 0.25 dex, and N with a range of 1.5 dex and steps of 0.3 dex. Since the spectrum is crowded with absorption lines that are broadened by rotation, we could not measure equivalent widths to determine the fundamental parameters. We performed the analysis of the different parameters by selecting wavelength regions that show a strong influence of these particular species. The final values were then derived using a χ^2 -method applied to the synthetic spectra grid for the selected regions.

4. Stellar parameters

4.1. Rotation

To determine $v_{\text{rot}} \sin i = 38 \pm 5$ km/s, we used a fit of a synthetic spectrum calculated with the literature values given by Miszalski et al. (2013b) and convolved with rotational profiles for values from $v_{\text{rot}} \sin i = 0$ to 50 km/s to two regions spanning from 6440 to 6515 Å and from 7030 to 7070 Å dominated by strong C_2 molecular absorption bands (Fig. 1).

4.2. Effective temperature and surface gravity

The many rotationally broadened lines in the observation also hamper the determination of equivalent widths. Thus, we used a set of diagnostic lines of Fe I, Fe II, Ti I, Ti II, Sc I, Sc II, and Mg I and performed a χ^2 -fit for selected wavelength regions. The set is composed of the lines that Taberner et al. (2018) used for a similar spectral analysis. Furthermore, we included some Fe I and

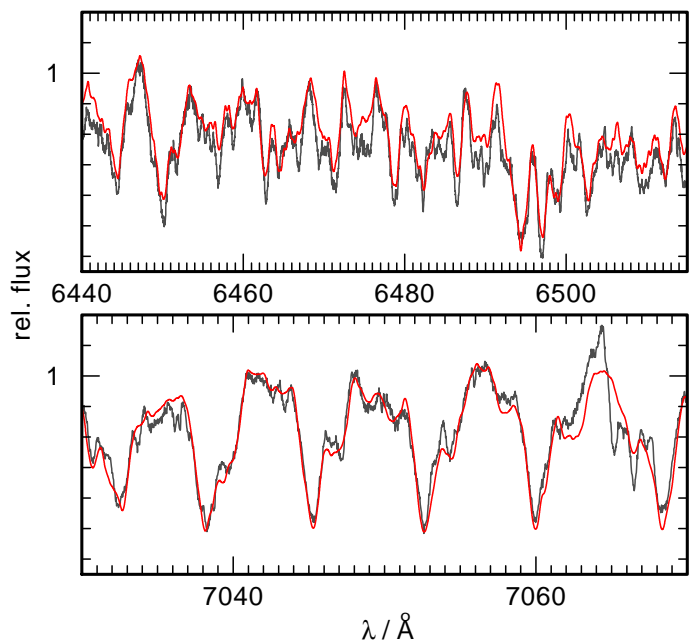


Fig. 1: Synthetic spectra (red) convolved with a rotational profile of $v_{\text{rot}} = 38$ km/s around strong C_2 and CN molecular absorption bands compared with observations (gray).

Fe II lines that are used by the Brussels Automatic Code for Characterizing High accuracy Spectra (BACCHUS⁶; Masseron et al. 2016). Finally, we added lines for Fe I, Fe II, Ti I, Ti II, Sc I, and Sc II for which we obtained the largest theoretical equivalent widths in the calculation of the synthetic spectra and that did not saturate. The resulting collection of wavelength regions used for the analysis and the list of diagnostic lines is shown in Table A.2. They cover a wide range of different excitation potentials and oscillator strengths. After a first determination of T_{eff} and $\log g$, we found a degeneracy in $\log g$ due to the fact that the strength of the computed lines in the regime around the literature values varies very little as a function of $\log g$ for a fixed value of T_{eff} . A spectroscopic determination of $\log g$ is hampered by uncertain values for the distance and brightness (Sect. 6.3). Thus, we adopt a value of $\log g = 2.5 \pm 0.5$ that is typical for Ba giants of that type (e.g., de Castro et al. 2016). This approach seems to be reasonable because a change of $\Delta \log g = 0.5$ only marginally affects the derived abundances compared to the significant statistical errors. We derive $T_{\text{eff}} = (4350 \pm 150)$ K. Fig. A.1 and Fig. A.2 illustrate the spectroscopic determination of these parameters by showing the difference due to a variation of T_{eff} and $\log g$.

5. Element abundances

We used model atmospheres with $T_{\text{eff}} = 4250$ K and $\log g = 2.5$ from the grid and performed line-profile fits for the following elements to determine their abundances. The results are given in Table 2. In our analysis, we assumed the atomic data to be correct and did not propagate uncertainties on atomic data. The continuum placement uncertainty is also assumed to be small as the continuum placement is shifted during the fitting procedure. To estimate the impact of a varied T_{eff} and $\log g$ on the determined abundances, we redid part of our analysis with models

⁶ <http://www.astro.ulb.ac.be/pmwiki/Spectro/Bacchus>

with varied T_{eff} between 4000 and 4500 K at $\log g$ varied between 2.0 and 3.0. We also varied the microturbulence velocity by ± 2.0 km/s, which was kept fixed at 2.0 km/s in the initial analysis. By far, the impact of a change in temperature is the largest. Compared to this error, the variation in $\log g$ and microturbulence velocity become negligible. Furthermore, we investigated the influence of the metallicity of the model atmosphere grid that was chosen for the analysis on the determined abundances and repeated part of the analysis with different input model metallicities between -0.5 and 0 . Raising (lowering) the metallicity by a certain amount results in a Fe abundance that is lower (higher) by roughly 1.3-fold that amount. Consistency is reached for the grid with $[M/H] = -0.3$ that gives a Fe abundance of $[\text{Fe}/\text{H}] = 0.3 \pm 1.0$. In our analysis, we find a C enrichment but cannot determine the O abundance and, thus, use the solar value. The resulting C/O ratio is larger than one. To test whether it is justified to use an O-rich model atmosphere grid (model 1) with solar abundances, we employed the ATLAS9 code and calculated a test model with a C abundance increased to the value found in our analysis (model 2). Furthermore, we calculated a second test model with the increased C abundance and an O abundance reduced by one dex (model 3). We redid the abundance analysis for C and Ba and found the same abundance for C from model 1 and 2. For the model with increased C and decreased O abundance, we get a C abundance that is 0.03 dex higher. Compared to model 1, the Ba abundance for model 2 is higher by 0.04 dex and by 0.2 dex for model 3. The difference between the O-rich model 1 and the C-rich model 2 is shown in Fig. A.3. The effect of the model atmosphere on the abundances is in a range that justifies relying on the available model atmosphere grid. Thus, we did not compute a C-rich grid. However, this adds another uncertainty to the abundances. We obtain large errors arising from the crowdedness of the observed spectrum that we estimate by detailed line profile fits and evaluation based on the χ -by-eye method. In many cases, this is the main contributor to the total error. It ranges between 0.05 dex for C and about 0.4 dex for the light metals up to about 1 dex for the iron group and trans-iron elements. To take the uncertainties in T_{eff} and $\log g$ into account, we did this procedure for the corners of the grid stated above ($T_{\text{eff}} = 4000$ K, $\log g = 3.0$ and 4500 K, 2.0). The abundance errors arising from this effect range between 0.03 dex for C to about 0.5 dex for the other metals. The total errors given in Table 2 are the maximum differences for the abundances that are possible within the error limits of this grid.

Carbon. We analyzed the C abundance using spectrum synthesis calculations for the region of strong C_2 absorption from 4650 \AA to 4737 \AA (Fig. 2). We confirm the C enhancement and our result of $[\text{C}/\text{H}] = 0.36 \pm 0.08$ agrees within 1σ with the value derived by Miszalski et al. (2013b) from their mid-resolution spectra.

Nitrogen. Using the C abundances, we derived the N abundance from synthetic calculations for the wavelength regions $7030\text{--}7070 \text{ \AA}$ and $7900\text{--}8100 \text{ \AA}$ affected by strong CN absorption bands. Fig. 3 shows the best result. We find N to be enriched to the same level as C with $[\text{N}/\text{H}] = 0.3 \pm 0.8$. We could not identify any line of oxygen in the observed spectrum and, thus, were unable to fix an abundance value for O. In our analysis, we adopt the solar value. To get an idea of the $^{12}\text{C}/^{13}\text{C}$ ratio, we analyzed the CN absorption band in the region $8100\text{--}8200 \text{ \AA}$ and included the line list for $^{13}\text{C}^{14}\text{N}$ from Sneden et al. (2014) (Fig. 4).

Table 2: Element abundances determined for Hen2–39 in $\log \epsilon = 12 + \log(n_X/n_{\text{H}})$, $[\text{X}/\text{H}] = \log(n_X/n_{\text{H}}) - \log(n_{\text{X},\odot}/n_{\text{H},\odot})$, and $[\text{X}/\text{Fe}] = \log(n_X/n_{\text{Fe}}) - \log(n_{\text{X},\odot}/n_{\text{Fe},\odot})$ with the number fraction n_X for element X.

Element	$\log \epsilon$	$[\text{X}/\text{H}]$	$[\text{X}/\text{Fe}]$	Error
C	8.9	0.36	0.71	0.08
N	8.3	0.3	0.7	0.8
Na	6.0	-0.3	0.1	0.7
Al	5.8	-0.7	-0.3	1.0
S	8.1	0.8	1.2	1.2
K	4.8	-0.3	0.1	1.0
Ca	5.9	-0.4	-0.1	1.0
Sc	< 2.4	< -0.7	< -0.4	
Ti	4.0	-0.9	-0.6	1.4
V	3.1	-0.9	-0.6	1.0
Cr	5.1	-0.5	-0.2	1.3
Mn	5.1	-0.3	0.0	1.0
Fe	7.1	-0.3		1.0
Co	5.1	0.2	0.5	1.0
Ni	6.5	0.2	0.6	1.3
Cu	5.0	0.8	1.2	1.5
Zn	< 5.8	< 1.2	< 1.6	
Rb	3.7	1.1	1.4	1.3
Sr	3.6	0.6	1.0	1.5
Y	2.3	0.0	0.4	1.5
Zr	2.4	-0.2	0.2	1.5
Nb	< 2.0	< 0.7	< 1.0	
Mo	2.9	1.0	1.4	1.3
Tc	< 2.5			
Ru	< 3.5	< 1.7	< 2.1	
Ba	3.6	1.4	1.8	0.5
La	2.3	1.1	1.5	1.6
Ce	< 3.5	< 2.0	< 2.3	
Pr	< 3.0	< 2.4	< 2.7	
Nd	1.9	0.4	0.8	1.5
Sm	< 1.7	< 0.8	< 1.1	
Eu	< 1.1	< 0.6	< 1.0	
Gd	< 2.6	< 1.5	< 1.8	
Tb	< 0.8	< 0.5	< 0.8	
Dy	< 4.5	< 3.4	< 3.8	
Er	< 2.4	< 1.6	< 1.9	
Hf	< 1.8	< 1.0	< 1.4	
W	1.4	0.7	1.1	1.5
Os	< 2.9	< 1.5	< 1.8	

From the inspection of the observation, we cannot claim to find an enhancement in ^{13}C resulting in $^{12}\text{C}/^{13}\text{C}$ lower than the solar value of 90, although this cannot be ruled out.

Light metals: Sodium to potassium. For the following elements, we used the most prominent absorption features in the synthetic spectra, which show the largest impact of a change of the abundance (Table A.3). The Na doublet $\text{Na I } \lambda\lambda 5890.8, 5896.5 \text{ \AA}$ (Fig. A.4) is used to find a Na abundance of $[\text{Na}/\text{Fe}] = 0.1 \pm 0.7$, which resembles well with the sample of Ba stars analyzed by de Castro et al. (2016, Fig. 6). From a fit to the regions affected by absorption due to Al we derive $[\text{Al}/\text{Fe}] = -0.3 \pm 1.0$. Ba stars typically show a slight enhancement in Al, which is also present in the sample

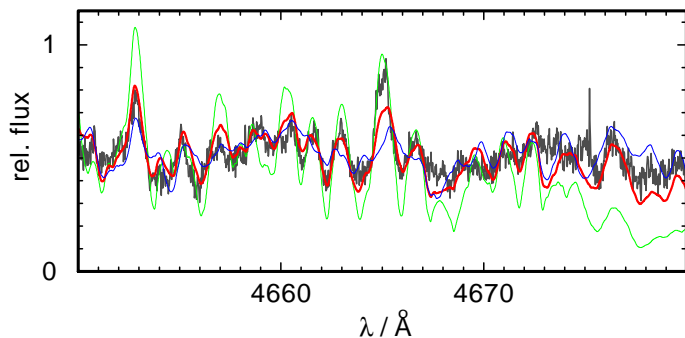


Fig. 2: Observation (gray) of Hen 2–39 compared to model spectra with $T_{\text{eff}}=4250$ K and $\log g = 2.5$ for a selected region of strong C_2 absorption for $[\text{C}/\text{H}] = 0.46, 0.36, 0.26$ (green, red, and blue, respectively).

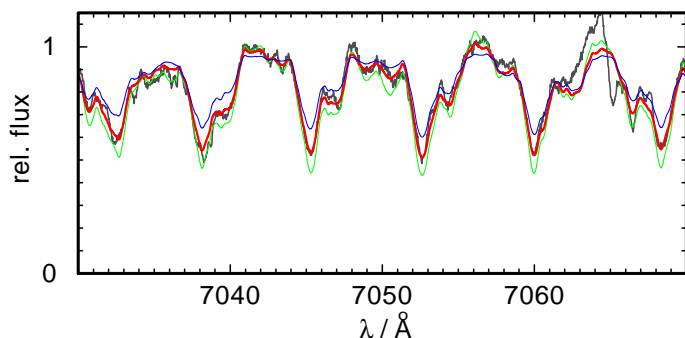


Fig. 3: Like Fig. 2, for strong CN absorption for $[\text{N}/\text{H}] = 1.1, 0.3, -0.5$ (green, red, and blue, respectively).

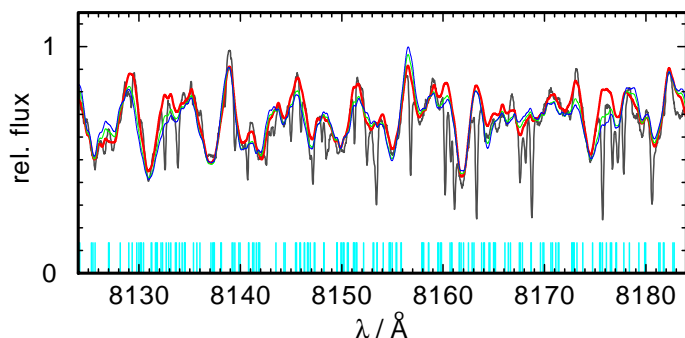


Fig. 4: Like Fig. 2, for strong CN absorption for $^{12}\text{C}/^{13}\text{C} = 90, 10, 5$ (red, green, and blue, respectively). ^{13}CN absorption lines are indicated at the bottom in cyan.

of de Castro et al. (2016). For S we derive $[\text{S}/\text{Fe}] = 1.2 \pm 1.2$ and for K we found $[\text{K}/\text{Fe}] = 0.1 \pm 1.0$.

Iron-peak elements: Calcium to copper. Selected absorption features due to neutral Ca to Cu are shown in Figs. A.5 and A.6. We performed a fit for a set of Fe I and Fe II absorption lines and found this star to be metal-poor with $[\text{Fe}/\text{H}] = -0.3 \pm 1.0$. For all iron-peak elements prior to Fe, we found solar values or slight underabundances, namely $[\text{Ca}/\text{Fe}] = -0.1 \pm 1.0$, $[\text{Ti}/\text{Fe}] = -0.6 \pm 1.4$, $[\text{V}/\text{Fe}] = -0.6 \pm 1.0$, $[\text{Cr}/\text{Fe}] = -0.2 \pm 1.3$, and $[\text{Mn}/\text{Fe}] = 0.0 \pm 1.0$. For Sc, we determined an upper limit of $[\text{Sc}/\text{Fe}] = -0.4$. These low values for the α elements Ca and Ti do not correspond with the trend in the sample of de Castro et al.

(2016) who found an enrichment of these elements compared to Fe with decreasing metallicity. The values close to solar for the other elements, however, are in good agreement with the sample showing a clustering of the abundances around $[\text{X}/\text{Fe}] = 0.0$. For the elements of this group subsequent to Fe, we determined overabundances compared to Fe of $[\text{Co}/\text{Fe}] = 0.5 \pm 1.0$, $[\text{Ni}/\text{Fe}] = 0.6 \pm 1.3$, and $[\text{Cu}/\text{Fe}] = 1.2 \pm 1.5$.

Trans-iron elements: Zinc to osmium. Selected wavelength regions that are among those showing the largest impact of a change in abundance for the elements of this group are shown in Figs. A.7–A.9. Since we found only few significant absorption features for the majority of these elements, the statistical errors of the determined values are large (often > 1 dex) and in many cases only upper abundance limits could be established. We obtained $[\text{Zn}/\text{Fe}] < 1.6$ and $[\text{Rb}/\text{Fe}] = 1.4 \pm 1.3$. For the elements around the first peak of the s-process, we found $[\text{Sr}/\text{Fe}] = 1.0 \pm 1.5$, $[\text{Y}/\text{Fe}] = 0.4 \pm 1.5$, and $[\text{Zr}/\text{Fe}] = 0.2 \pm 1.5$. Despite the large uncertainties, we find a good agreement with the Sr abundances of the sample of Karinkuzhi et al. (2018, Fig. 6). The Sr abundances for most of the Ba stars of Merle et al. (2016) are slightly lower but some reach up to 1 dex as well. Also the Y abundance of Hen 2–39 agrees well with the sample of Merle et al. (2016), whereas the majority of Ba giants of Karinkuzhi et al. (2018) and de Castro et al. (2016) crowd around higher values of Y. The $[\text{Zr}/\text{Fe}]$ abundances of Karinkuzhi et al. (2018) are significantly higher (all > 1 dex), whereas some of the Ba stars of Merle et al. (2016) agree with low values of $[\text{Zr}/\text{Fe}]$. Also the sample of de Castro et al. (2016) clusters around $[\text{Zr}/\text{Fe}] \approx 1$ but also shows stars with comparatively low values like that for Hen 2–39. For the elements subsequent to this peak, we determined $[\text{Nb}/\text{Fe}] < 1.0$, $[\text{Mo}/\text{Fe}] = 1.4 \pm 1.3$, and $[\text{Ru}/\text{Fe}] < 2.1$.

One key element of this analysis is the radioactive Tc. The strongest absorption features that appear in the synthetic spectra are $\text{Tc I } \lambda\lambda 4031.6, 4095.7, 4238.2, 4262.3, 4297.1 \text{ \AA}$. Unfortunately, these lines could not be clearly identified in the observed spectrum but it could be used to establish an upper abundance limit of $\log \epsilon_{\text{Tc}} < 2.5^7$.

For the determination of the Ba abundance, we used $\text{Ba II } \lambda\lambda 4554.0, 4931.1, 5853.7, 6141.7, 6496.9 \text{ \AA}$. The first two are very strong and sensitive to small variations of the abundance (Fig. A.8). This helped to constrain $[\text{Ba}/\text{Fe}] = 1.8 \pm 0.5$, which agrees within the error limits with the previous value of Miszalski et al. (2013b). The values determined by Karinkuzhi et al. (2018) for this element range from $0.81 \leq [\text{Ba}/\text{Fe}] \leq 2.67$. Also the sample of Merle et al. (2016) shows a scatter between almost solar and 2.5. Our strong enrichment found for Hen 2–39, thus, is not exceptional (Fig. 6).

La II absorption lines yield $[\text{La}/\text{Fe}] = 1.5 \pm 1.6$. For the other elements of the second peak of the s-process we found $[\text{Ce}/\text{Fe}] < 2.3$, $[\text{Pr}/\text{Fe}] < 2.7$, and $[\text{Nd}/\text{Fe}] = 0.8 \pm 1.5$. The upper limit for Ce lies above the value range of $1.02 \leq [\text{Ce}/\text{Fe}] \leq 1.76$ determined by Karinkuzhi et al. (2018) and also above that of Merle et al. (2016) ranging from solar to 1.5 dex. The Ba stars of de Castro et al. (2016) cluster around an enrichment of 1.0 dex and none of these stars reach values above 2.5 dex. Our upper limit for Pr lies above the value range of $1.18 \leq [\text{Pr}/\text{Fe}] \leq 2.55$ of Merle et al. (2016). However, our value for the Nd abundance is below their range of values. The star with the lowest Nd abundance shows $[\text{Nd}/\text{Fe}] = 1.18$, whereas the sample

⁷ $\log \epsilon = 12 + \log(n_{\text{X}}/n_{\text{H}})$

of de Castro et al. (2016) clustering around $[\text{Nd}/\text{Fe}] \approx 1.0$ perfectly agrees with our value within the error limits.

For the further rare-earth elements Sm, Eu, Gd, Tb, Dy, and Er, we could only establish upper abundance limits (Table 2). These elements are not analyzed by Merle et al. (2016) and de Castro et al. (2016). Karinkuzhi et al. (2018) found ranges of $1.02 \leq [\text{Sm}/\text{Fe}] \leq 2.17$, $0.96 \leq [\text{Eu}/\text{Fe}] \leq 1.43$, and $1.60 \leq [\text{Dy}/\text{Fe}] \leq 2.51$. Our upper limits of $[\text{Sm}/\text{Fe}] < 1.1$, and $[\text{Eu}/\text{Fe}] < 1.0$ lie within these ranges; $[\text{Dy}/\text{Fe}] < 3.8$ is significantly higher. Furthermore, we could determine the abundances of Hf, W, and Os to be $[\text{Hf}/\text{Fe}] < 1.4$, $[\text{W}/\text{Fe}] = 1.1 \pm 1.5$, and $[\text{Os}/\text{Fe}] < 1.8$.

6. Discussion

6.1. Element abundances

We compared our results with the yields from nucleosynthesis calculations of Karakas & Lugaro (2016) for a metallicity of $Z = 0.007$, in line with the low metallicity of $Z = 0.006$ that we determined from $Z = 10^{[\text{Fe}/\text{H}]} Z_{\odot}$ with $[\text{Fe}/\text{H}] = -0.3$ and $Z_{\odot} = 0.0134$ (Asplund et al. 2009). From these models and those of Karakas et al. (2018), it becomes obvious that AGB nucleosynthesis does not affect the abundances of the iron peak elements and, thus, it seems reasonable to assume the same low metallicity for both components of the binary.

The fact that we cannot see a ^{13}C enhancement agrees very well with the theoretical calculations predicting even an enhancement of the initial solar $^{12}\text{C}/^{13}\text{C}$ -ratio for models with initial masses $1.5 M_{\odot} \leq M_{\text{ini}} \leq 4.0 M_{\odot}$ where our estimated initial mass (Sect. 6.2) lies within.

The finding that the iron-peak elements prior to Fe show under-abundances and those subsequent to Fe are enhanced leads to the speculation that this pattern may be caused by neutron capture on the former elements as seed species and the formation of elements heavier than Fe. Fig. 5 also shows an enrichment due to AGB nucleosynthesis for the elements subsequent to Fe.

The observed N enhancement of $[\text{N}/\text{Fe}] = 0.7 \pm 0.8$ (Fig. 5) is in line with the enhancement found for the Ba stars of Karinkuzhi et al. (2018, Fig. 6). A high $[\text{N}/\text{C}]$ ratio as found for this object is discussed in the literature (e.g., Smiljanic et al. 2006; Merle et al. 2016). These authors argue that CN processing in Ba stars could result in higher N abundances. According to Smiljanic et al. (2006), an increased $[\text{N}/\text{C}]$ ratio can be caused by mixing events such as the first DU or by a more complex mixing process due to rotation for intermediate mass stars. This would be an indicator for hydrogen burning via the CNO-cycle in the stellar core. With the assumed mass for the primary star (Sect. 6.2), this should be the dominating fusion process in this star. The fast rotation of the Ba-CSPN is most likely due to transfer of angular momentum from the primary and therefore does not imply that this star was rotating exceptionally fast initially so as to affect its $[\text{N}/\text{C}]$ abundance ratio.

For Tc, we could not identify the presence of any line without doubt and, thus, cannot constrain the abundance further than $\log \epsilon_{\text{Tc}} < 2.5$. Therefore, we cannot claim this star to have Tc in its atmosphere, which would directly lead to the necessity of prior mass transfer. The models of Karakas & Lugaro (2016) predicted a final surface abundance between $\log \epsilon_{\text{Tc}} = 1.11$ and 1.24 for the models with initial masses between 2.1 and $2.5 M_{\odot}$, which lies well below the upper limit for Hen 2–39. Another diagnostic element reflecting recent s-process nucleosynthesis is Nb. According to Neyskens et al. (2015), this mono-isotopic species is synthesized by the decay of the radioactive

^{93}Zr produced by s-process nucleosynthesis. Compared to ^{99}Tc , this species has a longer half-life time of 1.53 Myr. Following our estimate made for Tc (Sect. 1), we do not expect a significant enrichment in Nb, since the primary's post-AGB age should be much shorter than the ^{93}Zr half-life and, thus, a large fraction of this species should still be present. Thus, the Nb/Zr would not represent the $^{93}\text{Zr}/\text{Zr}$ ratio at the end of the AGB and cannot be employed as proof for prior mass transfer. Furthermore, the Zr abundance can be determined only within a very large error range and for Nb, we find an upper limit only.

The detection of Tc is not hampered by the resolution of the spectrograph. The limiting factor is the S/N. We estimate the needed S/N that would be necessary to clearly distinguish between a model without Tc and one with $\log \epsilon_{\text{Tc}} = 1.2$. From Fig. 7, it becomes clear, that the current S/N is not sufficient to determine a Tc abundance of that level. Currently, the single spectra have a S/N of 3 at that wavelength region. This is increased by co-adding all the spectra, but still a S/N increased by a factor of 3 would be necessary. According to the UVES exposure time calculator (ETC), the needed S/N would require about a six fold longer exposure. For the future Extremely Large Telescope (ELT) the estimate is more promising. By using the E-ELT Spectroscopic ETC, we find that the required S/N is reached with an exposure of about half that of a single observation used in this analysis. For stars with a lower rotational velocity, the detection would become easier (Fig. 7). Unfortunately, all Ba CSPNe that are known up to now seem to rotate fast (shortest period of 4.7 d for Abell 70 and WeBo 1 and longest period of 5.9 d for LoTr 5; Bond et al. 2003; Miszalski et al. 2012; Aller et al. 2018), most likely because of the transfer of angular momentum by accretion of matter from the companion.

6.2. Mass transfer

By comparing our determined enrichment in s-process elements to the yields from evolutionary models for different initial masses of Karakas et al. (2018), we try to confirm that this can be the result of realistic mass transfer. For a primary that is currently in the stage of a CSPN, the secondary should have a mass that is lower by about 5% to be currently in the evolutionary stage of a red giant (assuming a mass dependent relation for the main-sequence lifetime $t \sim M^{-2.5}$). According to Joss et al. (1987), these stars should have a radiative core of about $0.3 M_{\odot}$ and a convective envelope of a mass $M_{\text{env}} = M_{\text{ini}} - 0.3 M_{\odot}$ within which the accreted mass becomes diluted. We want to determine a realistic mass range for the primary by comparing the total mass for the different elements that is ejected during the AGB evolution with the mass that the secondary would have needed to accrete to become that enriched. The mass of element X that needs to be accreted is given by $M_{\text{need}} = M_{\text{env}}(\text{mf}_{\text{X,final}} - \text{mf}_{\text{X,initial}})$ with a final mass fraction $\text{mf}_{\text{X,final}}$ according to our analysis results and an initial mass fraction $\text{mf}_{\text{X,initial}}$ according to the low metallicity. In Fig. 8, we show the needed mass compared to the total ejected mass for C, N, and the elements heavier than Fe that show a significant production due to AGB nucleosynthesis. Since most of the abundances could not be constrained within small error limits, we focus on the C and Ba abundances. For all models of Fig. 8 and some additional models, we calculated the percentage of the total ejecta that would need to be accreted to produce the observed enrichment (Table 3). It is obvious that only the models for an initial mass between 1.5 and $4.0 M_{\odot}$ can explain the enrichment due to a realistic mass transfer. For the models with the lowest initial masses as well as for those with the highest masses, the ratio of

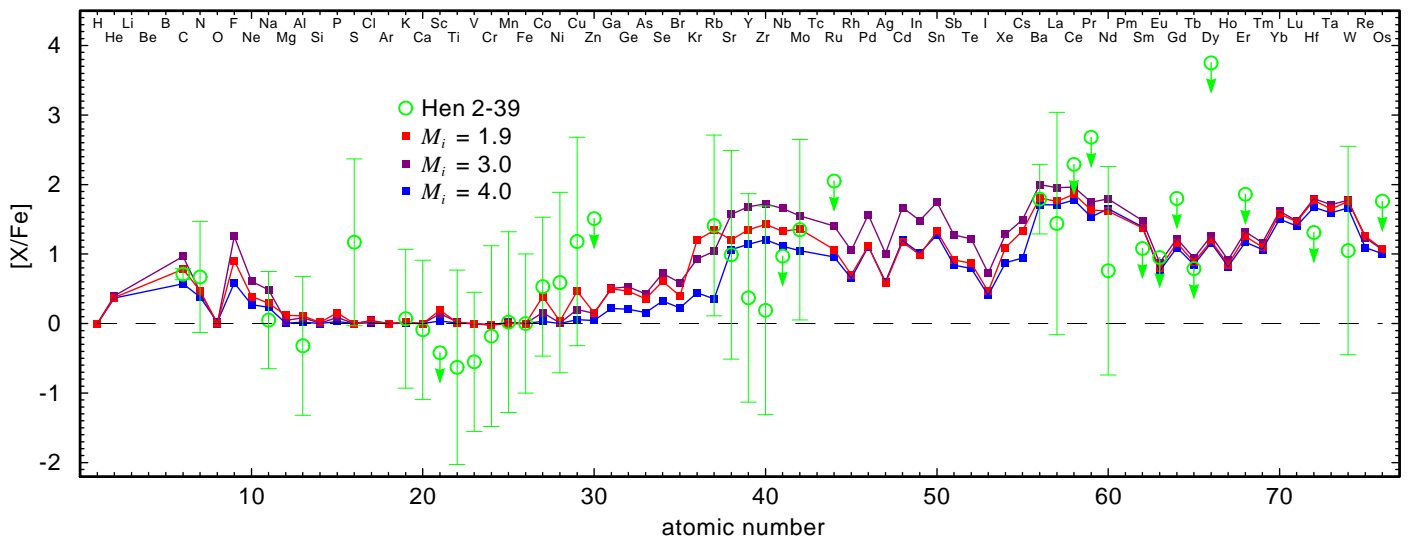


Fig. 5: Atmospheric element abundances of Hen 2–39 compared to the final yields of a selection of evolutionary models from Karakas & Lugaro (2016) with a metallicity of $Z = 0.007$. The initial masses are indicated in the upper panel. Arrows indicate upper limits.

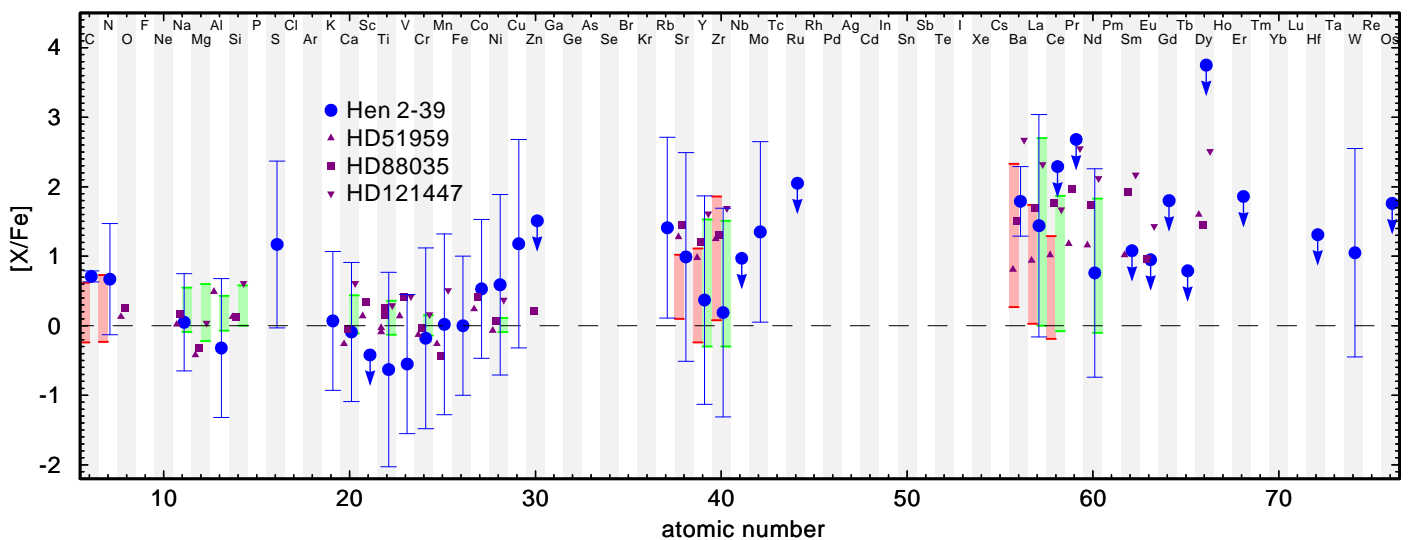


Fig. 6: Atmospheric element abundances of Hen 2–39 (blue) compared to the values for the three Ba stars HD51959, HD88035, and HD121447 analyzed by Karinkuzhi et al. (2018, (purple)) and the ranges that Merle et al. (2016, (red)) and de Castro et al. (2016, (green)) found for their sets of Ba-stars. Arrows indicate upper limits.

the yield of Ba to that of C is smaller, i.e., these models produce a smaller amount of Ba compared to C. The fraction of accreted mass of C and Ba should be equal. Thus, a 1.75–3.00 M_{\odot} progenitor seems to be most consistent with the abundance determinations. For this analysis, we used the models with the largest ^{13}C -pocket that are available from Karakas & Lugaro (2016). The larger the pocket size, the lower the yield of C and the higher that of Ba, i.e., the ratio of the yield of Ba to that of C is larger. Even for the models with the largest ^{13}C -pocket, the percentage of the total ejecta that would need to be accreted is higher considering the Ba abundance compared to the C abundance. This ratio becomes worse for smaller pocket sizes. In addition to the choice of the ^{13}C -pocket, yields of the evolutionary models are affected by uncertainties due to mass loss, convective mixing, reaction rates, and neutron poisons (Karakas & Lattanzio 2014). These effects are not evaluated by Karakas & Lugaro (2016) and we take the tabulated yields without considering an error range.

However, the progenitor mass estimate is affected by large uncertainties on the abundances and on the model yields and, thus, should be treated with caution.

This result leads to the conclusion that even such a high enrichment can reasonably be explained with realistic mass-transfer mechanisms such as wind-RLOF (Chen et al. 2017). In this scenario only a small fraction of mass becomes unbound from the binary and the percentage of accreted mass ranges between 20 and 40%. Simulations indicate that a binary with a wide separation, where mass transfer would act via the Bondi-Hoyle mechanism, can be ruled out since the percentage of accreted mass decreases to only 2 to 3% (Theuns et al. 1996). CE evolution would imply a short orbital period (\leq a few days), which is not the case for this binary and, thus, this scenario is also ruled out.

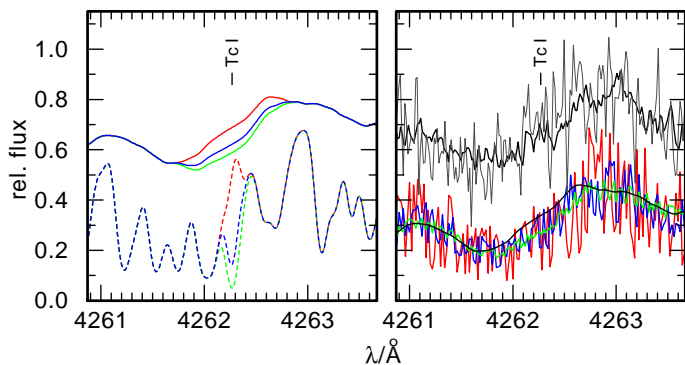


Fig. 7: Left panel: Comparison between models with $\log \epsilon_{Tc} = 0.0, 1.2, 2.5$ (red, blue, green) for models broadened with a rotational profile ($v_{\text{rot}} = 36$ km/s, solid lines with 0.35 offset) and without rotation (dashed). Right: Comparison between a rotationally broadened model without Tc (black) and models with $\log \epsilon_{Tc} = 1.2$ with different levels of artificial noise (S/N of the single observation: red, S/N of co-added spectrum: blue, required S/N: green). For comparison, the observation is shown with an offset of 0.35 (single spectrum: gray, co-added spectra: black).

Table 3: Percentage of the total ejecta that would need to be accreted to produce the observed enrichment of Hen 2–39 for evolutionary models of Karakas & Lugaro (2016) with $Z = 0.007$ for different initial masses.

M_{ini}/M_{\odot}	C	Ba
1.00	156	2215
1.50	49	94
1.75	25	36
1.90	26	32
2.10	14	17
2.25	15	18
2.50	12	15
2.75	9	15
3.00	10	15
3.50	12	24
4.00	18	27
5.00	89	1311

6.3. Spectroscopic distance

For Hen 2–39, several different distances are published. The nebular analysis of Miszalski et al. (2013b) yields 5.7 kpc. Frew et al. (2016) found $7.6^{+1.5}_{-1.3}$ kpc based on the companion spectral type. The CSPN of Hen 2–39 is in the Gaia data release (DR2, ID: 5256396485463285504, Gaia Collaboration 2018).

The parallax of 0.0564 ± 0.0340 mas is affected by a large error corresponding to relative errors of 60.3%. The object is also contained in the catalog of distances of Bailer-Jones et al. (2018) derived from the DR2 data. They found $9.071^{+2.939}_{-1.962}$ kpc. With our result for the companion mass, we would like to get a clue for the distance for the binary in Hen 2–39. Using the assumed giant $\log g = 2.5$, the derived mass of about $2.2 M_{\odot}$ for the Ba star, and the determined T_{eff} , we get

$$M_{\text{bol}} = M_{\text{bol},\odot} + 2.5 (\log g - \log g_{\odot}) - 2.5 \log \left(\frac{M}{M_{\odot}} \right) - 10 \log \left(\frac{T_{\text{eff}}}{T_{\text{eff},\odot}} \right) = 0.262.$$

The solar values are taken from the *Sun Facts Sheet* from the NASA Goddard Space Flight Center⁸ and we use $M_{\text{bol},\odot} = 4.74$ mag for the Sun derived from the standardized absolute bolometric magnitude scale defined by the international astronomical union (Mamajek et al. 2015). The error of M_{bol} is dominated by the uncertainty of $\log g$. Assuming an uncertainty of $\Delta \log g = 0.5$ and $\Delta M = 0.5 M_{\odot}$, we get $\Delta M_{\text{bol}} = 1.316$. Nevertheless, we can derive the absolute visual magnitude $M_V = M_{\text{bol}} - BC(V) = 0.852 \pm 1.525$. The bolometric correction of $BC(V) = -0.590 \pm 0.209$ is calculated using the approach of Alonso et al. (1999) including the preliminary values for T_{eff} and the Fe abundance.

We can now estimate the distance via the distance modulus but the known V magnitude shows a much larger uncertainty than the more recent infrared magnitudes (Table 4). By comparing the calculated flux normalized on the K magnitude of Cutri et al. (2003) with the B and V magnitudes of Tylden et al. (1991) and those for the I, J , and K bands from Epchtein et al. (1999), it becomes obvious that our model agrees very well with the brightness values in all filters (Fig. 9). Thus, we decided to rely on the precise I magnitude for the distance estimation. Using the color relation for $(V - I)$ from Alonso et al. (1999) for the given T_{eff} , we find $(V - I) = 1.543^{+0.124}_{-0.110}$ mag. This leads to an absolute M_I brightness of $M_I = -0.691^{+1.635}_{-1.649}$ mag.

Miszalski et al. (2013b) determined an extinction of $E_{B-V} = 0.37$ mag. With the Galactic extinction law with $R_V = 3.1$ and the relation from Cardelli et al. (1989), we derive the total absorption for the I band of $A_I = 0.5A_V = 0.5 \times 3.1E_{B-V} = 0.565$ mag. Now, we find $d = 10^{-(M_I - I + A_I - 5)/5} = 9.15^{+10.65}_{-4.90}$ kpc. The large error is again an effect of the assumed uncertainty in $\log g$ but, nevertheless, the value agrees with all other distance values within these limits. Furthermore, this value is very close to that derived from the GAIA parallax measurement. With a precise distance measurement, we could get a second handle on the mass of the Ba star. The mass could then be derived by comparing its properties to evolutionary tracks for different masses and compared with our value derived using the abundance yields of evolutionary models.

With its Galactic latitude of -4.239° (Gaia Collaboration 2018), the star is located $0.676^{+0.789}_{-0.362}$ kpc below the Galactic plane, which means that it is just below the edge of the Galactic thin disk (Rix & Bovy 2013) and, thus, should belong to the thick disk. This assignment is in agreement with the observed low metallicity since simulations for the Galactic metallicity distribution predict negative metallicity gradients for low scale heights and may change the sign at about a scale height of 1.5 kpc. Ivezić et al. (2012) also found thick disk stars to be more metal poor (median $[\text{Fe}/\text{H}] = -0.6$) compared to thin disk stars (median $[\text{Fe}/\text{H}] = -0.2$), where Hen 2–39 lies just in the middle. Furthermore, we can use M_{bol} to estimate the luminosity $L/L_{\odot} = 10^{(M_{\text{bol},\odot} - M_{\text{bol}})/2.5} = 61.83^{+145.95}_{-43.43}$ and the radius

$$\frac{R}{R_{\odot}} = \sqrt{\frac{L}{L_{\odot}} \frac{T_{\text{eff},\odot}^4}{T_{\text{eff}}^4}} = 13.84^{+13.38}_{-6.78}.$$

Using the rotational velocity from Section 4.1 and the radius the star should have a rotational period of 18.4 d for a high inclination of $i = 90^\circ$. Miszalski et al. (2013b) detected a photometric variability of the star with a period of 5.46 d. Assuming this value for the rotation, we can find an inclination of $i = 17.22^{+18.30}_{-8.53}$. The parameters are summarized in Table 5.

⁸ <https://nssdc.gsfc.nasa.gov/planetary/factsheet/sunfact.html> Version 29-06-2018.

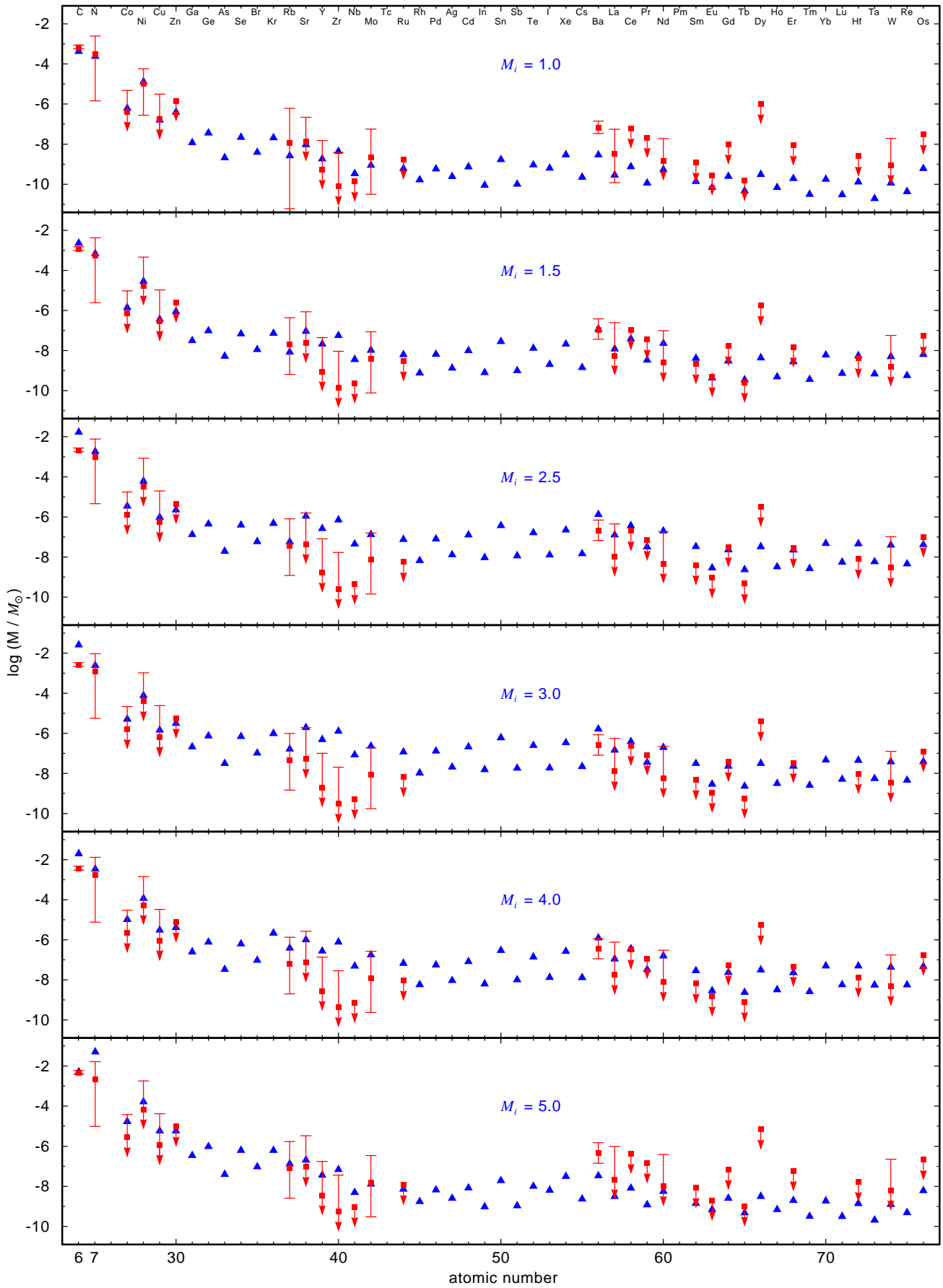


Fig. 8: Total amount of mass ejected during AGB evolution of different elements for evolutionary models from Karakas & Lugaro (2016) for $Z = 0.007$ with initial masses of 1.0 to $5.0 M_\odot$ (blue, initial mass indicated in the panel) compared to the need of accreted mass to reproduce the determined abundance values of the secondary via mass transfer (red).

Table 4: Brightnesses in different filters for the Ba CSPN of Hen 2–39.

Filter	Magnitude	Reference
<i>B</i>	17.9 ± 0.5	Tylenda et al. (1991)
<i>V</i>	16.5 ± 0.5	Tylenda et al. (1991)
<i>I</i>	14.68 ± 0.03	Epchtein et al. (1999)
<i>J</i>	13.474 ± 0.033	Cutri et al. (2003)
<i>H</i>	12.614 ± 0.033	Cutri et al. (2003)
<i>K</i>	12.338 ± 0.030	Cutri et al. (2003)

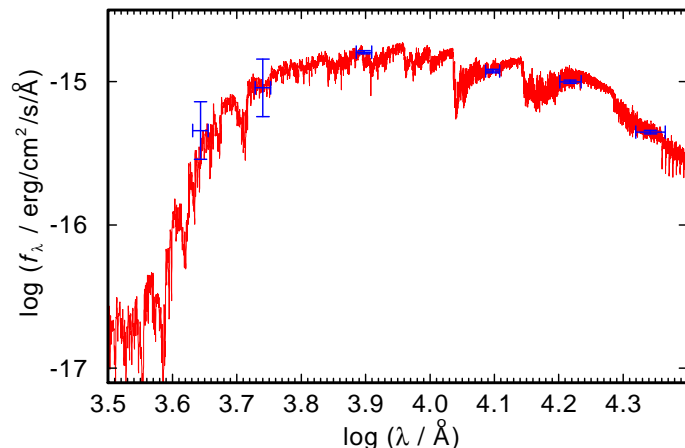


Fig. 9: Synthetic spectrum of our best model of Hen 2–39 normalized to the *H* magnitude of Cutri et al. (2003) and convolved with a Gaussian with FWHM = 5 Å for clarity, including interstellar reddening with $E_{B-V} = 0.37$ (red) compared with the observed magnitudes (Table 4).

Table 5: Properties of the CSPN of Hen 2–39.

T_{eff}	(4350 ± 150) K
distance ^a	5.7 kpc
distance ^b	$(9.071^{+2.939}_{-1.962})$ kpc
distance	$(9.15^{+10.65}_{-4.90})$ kpc
BC(<i>V</i>)	(-0.590 ± 0.209) mag
M_{bol}	0.262 ± 1.316
$(V - I)_0$	$1.543^{+0.124}_{-0.110}$
$E(B - V)^a$	-0.37
L/L_{\odot}	$61.83^{+145.95}_{-43.43}$
M/M_{\odot}	2.2 ± 0.5
log <i>g</i>	2.5 ± 0.5
R/R_{\odot}	$13.84^{+13.38}_{-6.78}$
rotation period ^a	5.46 d
$v_{\text{rot}} \sin i$	38 ± 5 km/s
<i>i</i>	$(17.22^{+18.30}_{-8.53})^{\circ}$

Notes.

^(a) Miszalski et al. (2013b) ^(b) Bailer-Jones et al. (2018)

We speculate that the rotational axis of the giant is perpendicular to the binary orbital plane. The low inclination is then in good agreement with the ring-like appearance of the nebula (Miszalski et al. 2013b), which indicates a nearly pole-on view and therefore a binary orbital plane almost in the plane of the sky (Hillwig et al. 2016).

7. Summary and conclusions

We presented and discussed the spectral analysis of UVES spectra of the Ba CSPN of Hen 2–39. Within the error limits, we confirm the result of Miszalski et al. (2013b) that the observed nucleus of Hen 2–39 has a cool atmosphere of $T_{\text{eff}} = (4350 \pm 150)$ K. Furthermore, we confirm the C and Ba enrichment but can significantly improve the abundances of $[C/H] = 0.36 \pm 0.08$ and $[Ba/Fe] = 1.8 \pm 0.50$ due to the high resolution of the analyzed spectra. We determined abundances or upper abundance limits for 26 trans-iron elements for the first time. For Tc, the lightest element with no stable isotope, we find an upper abundance limit of $\log \epsilon_{\text{Tc}} < 2.5$. This does not confirm the presence of Tc in the atmosphere of the star proving prior mass transfer. The limiting factor is not the resolution of the spectrum. For a clear detection of Tc, an exposure time about six times longer than that of all the spectra combined would be required to obtain the necessary S/N ratio. We can find a low metallicity of $[Fe/H] = -0.3 \pm 1.0$ for the Ba giant. The determined abundance pattern requires mass transfer from a companion with an extremely high enrichment of AGB nucleosynthesis products. The comparison with nucleosynthesis models of Karakas & Lugaro (2016) indicates an initial mass of 1.75–3.00 M_{\odot} for the primary. The percentage of ejected mass that needs to be accreted indicates that the preferred mass transfer mechanism is wind-RLOF. A wide binary involving Bondi-Hoyle accretion can be ruled out as can a CE evolution. For this star, the distance is rather uncertain. Thus, it cannot be used for a spectroscopic determination of the mass by interpolation from evolutionary tracks. A precise spectroscopic determination of the distance is hampered by the fact that log *g* cannot be constrained within narrow error limits from the analysis of the spectra. It is highly desirable to get a more precise distance measurement. This would also help to get a second value for the mass of the Ba CSPN to compare with that derived from the comparison with AGB models. With this second measurement, it would be possible to refine the primary mass estimate and place stronger constraints on the mass transfer. Our result for the height above the Galactic plane places this system among the thick disk population, in good agreement with the subsolar metallicity derived by our analysis.

Acknowledgements. We thank the anonymous referee for their constructive review of the manuscript. We thank Brent Miszalski and Thomas Rauch for their helpful comments and suggestions. LL is supported by the German Research Foundation (DFG, grant WE1312/49-1) and by the Studentship Programme of the European Southern Observatory. DJ gratefully acknowledges the Spanish Ministry of Economy and Competitiveness (MINECO) under the grant AYA2017-83383-P. This research has made use of NASA’s Astrophysics Data System and the SIMBAD database, operated at CDS, Strasbourg, France. This work has made use of data from the European Space Agency (ESA) mission *Gaia* (<https://www.cosmos.esa.int/gaia>), processed by the *Gaia* Data Processing and Analysis Consortium (DPAC, <https://www.cosmos.esa.int/web/gaia/dpac/consortium>). Funding for the DPAC has been provided by national institutions, in particular the institutions participating in the *Gaia* Multilateral Agreement.

References

- Abate, C., Pols, O. R., Izzard, R. G., Mohamed, S. S., & de Mink, S. E. 2013, *A&A*, 552, A26
- Acker, A., Marcout, J., Ochsenbein, F., et al. 1992, *The Strasbourg-ESO Catalogue of Galactic Planetary Nebulae. Parts I, II.*
- Aller, A., Lillo-Box, J., Vučković, M., et al. 2018, *MNRAS*, 476, 1140
- Alonso, A., Arribas, S., & Martínez-Roger, C. 1999, *A&AS*, 140, 261
- Asplund, M., Grevesse, N., Sauval, A. J., & Scott, P. 2009, *ARA&A*, 47, 481
- Bailer-Jones, C. A. L., Rybizki, J., Fouesneau, M., Mantelet, G., & Andrae, R. 2018, *AJ*, 156, 58

Table A.1: Observation log for the UVES observations.

Bidelman, W. P. & Keenan, P. C. 1951, *ApJ*, 114, 473
Blanco-Cuaresma, S., Soubiran, C., Heiter, U., & Jofré, P. 2014, *A&A*, 569, A111
Boffin, H. M. J. 2015, *Ecology of Blue Straggler Stars*
Boffin, H. M. J. & Jorissen, A. 1988, *A&A*, 205, 155
Bond, H. E., Pollacco, D. L., & Webbink, R. F. 2003, *AJ*, 125, 260
Buckley, D. A. H., Swart, G. P., & Meiring, J. G. 2006, in *Proc. SPIE*, Vol. 6267, *Society of Photo-Optical Instrumentation Engineers (SPIE) Conference Series*, 62670Z
Burgh, E. B., Nordsieck, K. H., Kobulnicky, H. A., et al. 2003, in *Proc. SPIE*, Vol. 4841, *Instrument Design and Performance for Optical/Infrared Ground-based Telescopes*, ed. M. Iye & A. F. M. Moorwood, 1463–1471
Cardelli, J. A., Clayton, G. C., & Mathis, J. S. 1989, *ApJ*, 345, 245
Castelli, F. & Kurucz, R. L. 2003, in *IAU Symposium*, Vol. 210, *Modelling of Stellar Atmospheres*, ed. N. Piskunov, W. W. Weiss, & D. F. Gray, A20
Chen, Z., Frank, A., Blackman, E. G., Nordhaus, J., & Carroll-Nellenback, J. 2017, *MNRAS*, 468, 4465
Corradi, R. L. M., Sabin, L., Miszalski, B., et al. 2011, *MNRAS*, 410, 1349
Cutri, R. M., Skrutskie, M. F., van Dyk, S., et al. 2003, *VizieR Online Data Catalog*, II/246
de Castro, D. B., Pereira, C. B., Roig, F., et al. 2016, *MNRAS*, 459, 4299
De Marco, O. 2009, *PASP*, 121, 316
Dekker, H., D’Odorico, S., Kaufer, A., Delabre, B., & Kotzlowski, H. 2000, in *Proc. SPIE*, Vol. 4008, *Optical and IR Telescope Instrumentation and Detectors*, ed. M. Iye & A. F. M. Moorwood, 534–545
Epchtein, N., Deul, E., Derriere, S., et al. 1999, *VizieR Online Data Catalog*, 2240
Frew, D. J., Parker, Q. A., & Bojčić, I. S. 2016, *MNRAS*, 455, 1459
Gaia Collaboration. 2018, *VizieR Online Data Catalog*, 1345
Gray, R. O. & Corbally, C. J. 1994, *AJ*, 107, 742
Gray, R. O., McGahee, C. E., Griffin, R. E. M., & Corbally, C. J. 2011, *AJ*, 141, 160
Grevesse, N. & Sauval, A. J. 1998, *Space Sci. Rev.*, 85, 161
Han, Z., Eggleton, P. P., Podsiadlowski, P., & Tout, C. A. 1995, *MNRAS*, 277, 1443
Henize, K. G. 1967, *ApJS*, 14, 125
Herwig, F. 2005, *ARA&A*, 43, 435
Hillwig, T. C., Jones, D., De Marco, O., et al. 2016, *ApJ*, 832, 125
Hubeny, I., Mihalas, D., & Werner, K., eds. 2003, *Astronomical Society of the Pacific Conference Series*, Vol. 288, *Stellar Atmosphere Modeling*
Husti, L., Gallino, R., Bisterzo, S., Straniero, O., & Cristallo, S. 2009, *PASA*, 26, 176
Iben, Jr., I. & Livio, M. 1993, *PASP*, 105, 1373
Ivezić, Ž., Beers, T. C., & Jurić, M. 2012, *ARA&A*, 50, 251
Jones, D. & Boffin, H. M. J. 2017, *Nature Astronomy*, 1, 0117
Jones, D., Van Winckel, H., Aller, A., Exter, K., & De Marco, O. 2017, *A&A*, 600, L9
Jorissen, A. & Mayor, M. 1988, *A&A*, 198, 187
Jorissen, A., Van Eck, S., Mayor, M., & Udry, S. 1998, *A&A*, 332, 877
Joss, P. C., Rappaport, S., & Lewis, W. 1987, *ApJ*, 319, 180
Karakas, A. I. & Lattanzio, J. C. 2014, *PASA*, 31, e030
Karakas, A. I. & Lugaro, M. 2016, *ApJ*, 825, 26
Karakas, A. I., Lugaro, M., Carlos, M., et al. 2018, *MNRAS*, 477, 421
Karinkuzhi, D., Goswami, A., Sridhar, N., Masseron, T., & Purandardas, M. 2018, *MNRAS*, 476, 3086
Kobulnicky, H. A., Nordsieck, K. H., Burgh, E. B., et al. 2003, in *Proc. SPIE*, Vol. 4841, *Instrument Design and Performance for Optical/Infrared Ground-based Telescopes*, ed. M. Iye & A. F. M. Moorwood, 1634–1644
Kurucz, R. L. 1991, in *NATO ASIC Proc. 341: Stellar Atmospheres - Beyond Classical Models*, ed. L. Crivellari, I. Hubeny, & D. G. Hummer, 441
Lebzelter, T. & Hron, J. 2003, *A&A*, 411, 533
Madonna, S., Bautista, M. A., Dinerstein, H., et al. 2018, *ArXiv e-prints*
Madonna, S., García-Rojas, J., Sterling, N. C., et al. 2017, *MNRAS*, 471, 1341
Mamajek, E. E., Torres, G., Prsa, A., et al. 2015, *ArXiv e-prints*
Masseron, T., Merle, T., & Hawkins, K. 2016, *BACCHUS: Brussels Automatic Code for Characterizing High accuracy Spectra*, *Astrophysics Source Code Library*
McClure, R. D. 1983, *ApJ*, 268, 264
McClure, R. D., Fletcher, J. M., & Nemeč, J. M. 1980, *ApJ*, 238, L35
McClure, R. D. & Woodsworth, A. W. 1990, *ApJ*, 352, 709
Merle, T., Jorissen, A., Van Eck, S., Masseron, T., & Van Winckel, H. 2016, *A&A*, 586, A151
Merrill, P. W. 1952, *ApJ*, 116, 21
Miller Bertolami, M. M. 2016, *A&A*, 588, A25
Miszalski, B., Boffin, H. M. J., & Corradi, R. L. M. 2013a, *MNRAS*, 428, L39
Miszalski, B., Boffin, H. M. J., Frew, D. J., et al. 2012, *MNRAS*, 419, 39
Miszalski, B., Boffin, H. M. J., Jones, D., et al. 2013b, *MNRAS*, 436, 3068
Mohamed, S. & Podsiadlowski, P. 2007, in *Astronomical Society of the Pacific Conference Series*, Vol. 372, *15th European Workshop on White Dwarfs*, ed. R. Napiwotzki & M. R. Burleigh, 397

Start Time (UT)	$\lambda / \text{\AA}$	Exp. Time/s	S/N
2014-04-03 02:42:47	5654–9465	1500	14.8
2014-04-03 02:42:51	3732–5000	1500	3.7
2014-04-03 03:08:39	5654–9465	1500	14.1
2014-04-03 03:08:39	3732–5000	1500	3.3
2014-04-03 03:36:22	5654–9465	1500	12.6
2014-04-03 03:36:26	3732–5000	1500	3.1
2014-04-03 04:02:13	5654–9465	1500	14.5
2014-04-03 04:02:14	3732–5000	1500	3.7
2014-04-04 00:40:42	5654–9465	1500	13.5
2014-04-04 00:40:46	3732–5000	1500	3.1
2014-04-04 01:06:34	5654–9465	1500	13.1
2014-04-04 01:06:34	3732–5000	1500	2.9
2014-04-04 01:34:52	5654–9465	1500	14.8
2014-04-04 01:34:59	3732–5000	1500	3.7
2014-04-04 02:00:47	3732–5000	1500	3.5
2014-04-04 02:00:47	5654–9465	1500	14.8
2014-04-04 02:32:05	5654–9465	1500	14.5
2014-04-04 02:32:11	3732–5000	1500	3.2
2014-04-04 02:57:59	3732–5000	1500	3.3
2014-04-04 02:58:00	5654–9465	1500	14.1
2014-04-13 02:30:36	5654–9465	1450	12.9
2014-04-13 02:30:40	3732–5000	1450	2.9
2014-04-13 02:55:38	3732–5000	1450	3.2
2014-04-13 02:55:39	5654–9465	1450	13.7
2014-04-15 00:20:10	5654–9465	1450	14.3
2014-04-15 00:20:14	3732–5000	1450	3.0
2014-04-15 00:45:11	5654–9465	1450	11.3
2014-04-15 00:45:12	3732–5000	1450	2.4
2014-04-15 01:10:37	5654–9465	1450	12.9
2014-04-15 01:10:41	3732–5000	1450	2.7
2014-04-15 01:35:39	3732–5000	1450	2.9
2014-04-15 01:35:39	5654–9465	1450	13.4
2014-04-15 02:01:20	5654–9465	1500	13.1
2014-04-15 02:01:24	3732–5000	1500	2.8
2014-04-15 02:27:11	5654–9465	1500	13.1
2014-04-15 02:27:12	3732–5000	1500	2.6

Nagai, T., Oka, K., Matsuda, T., et al. 2004, *A&A*, 419, 335
Neyskens, P., van Eck, S., Jorissen, A., et al. 2015, *Nature*, 517, 174
Palmeri, P., Quinet, P., Biéumont, É., et al. 2007, *MNRAS*, 374, 63
Rix, H.-W. & Bovy, J. 2013, *A&A Rev.*, 21, 61
Saladino, M. I., Pols, O. R., van der Helm, E., Pelupessy, I., & Portegies Zwart, S. 2018, *ArXiv e-prints*
Smiljanic, R., Barbuy, B., de Medeiros, J. R., & Maeder, A. 2006, in *Revista Mexicana de Astronomia y Astrofisica Conference Series*, Vol. 26, *Revista Mexicana de Astronomia y Astrofisica Conference Series*, 45–46
Snedden, C., Lucatello, S., Ram, R. S., Brooke, J. S. A., & Bernath, P. 2014, *The Astrophysical Journal Supplement Series*, 214, 26
Taberner, H. M., Dorda, R., Negueruela, I., & González-Fernández, C. 2018, *MNRAS*, 476, 3106
Theuns, T., Boffin, H. M. J., & Jorissen, A. 1996, *MNRAS*, 280, 1264
Thevenin, F. & Jasiewicz, G. 1997, *A&A*, 320, 913
Tyndall, R., Acker, A., Stenholm, B., Gleizes, F., & Raytchev, B. 1991, *A&AS*, 89, 77
Tyndall, A. A., Jones, D., Boffin, H. M. J., et al. 2013, *MNRAS*, 436, 2082
Van Eck, S. & Jorissen, A. 1999, *A&A*, 345, 127
Werner, K. & Herwig, F. 2006, *PASP*, 118, 183
Wray, J. D. 1966, PhD thesis, Northwestern University.

Appendix A: Additional figures and tables.

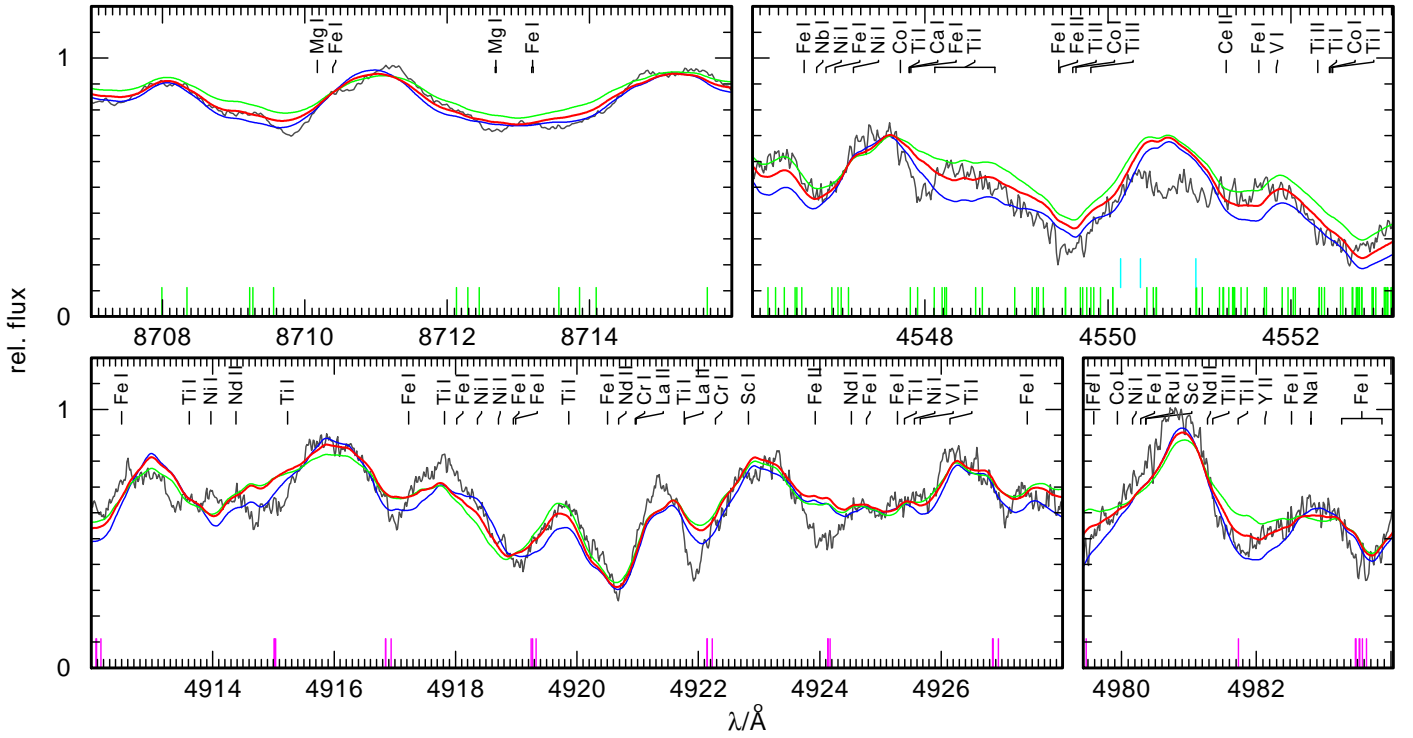


Fig. A.1: Observation (gray) of Hen 2–39 compared to model spectra with $T_{\text{eff}} = 4000, 4250, 4500\text{K}$ (blue, red, green) for selected regions that were used for the determination of T_{eff} . CN, C₂, and CH absorption lines are indicated at the bottom in green, purple, and cyan, respectively. All absorption lines that appear with an equivalent width $\geq 20\text{ mÅ}$ in the calculated spectrum are indicated.

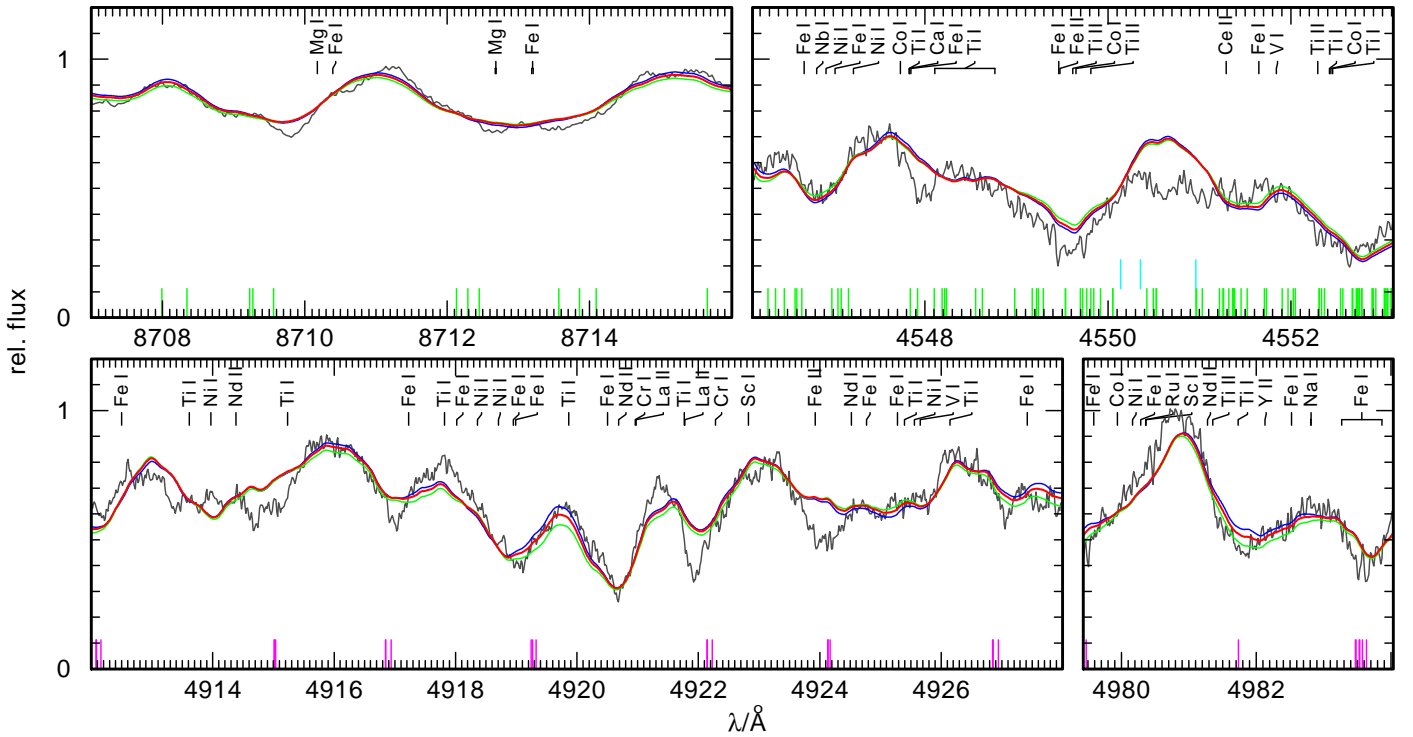


Fig. A.2: Like Fig. A.1, for $\log g = 2.0, 2.5, 3.0$ (blue, red, green).

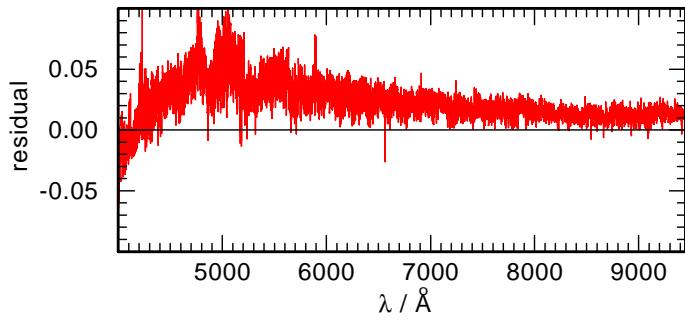


Fig. A.3: Difference between the newly computed C-rich test model (model 2) and the O-rich model from the available grid (model 1) for $T_{\text{eff}} = 4250$ K and $\log g = 2.5$.

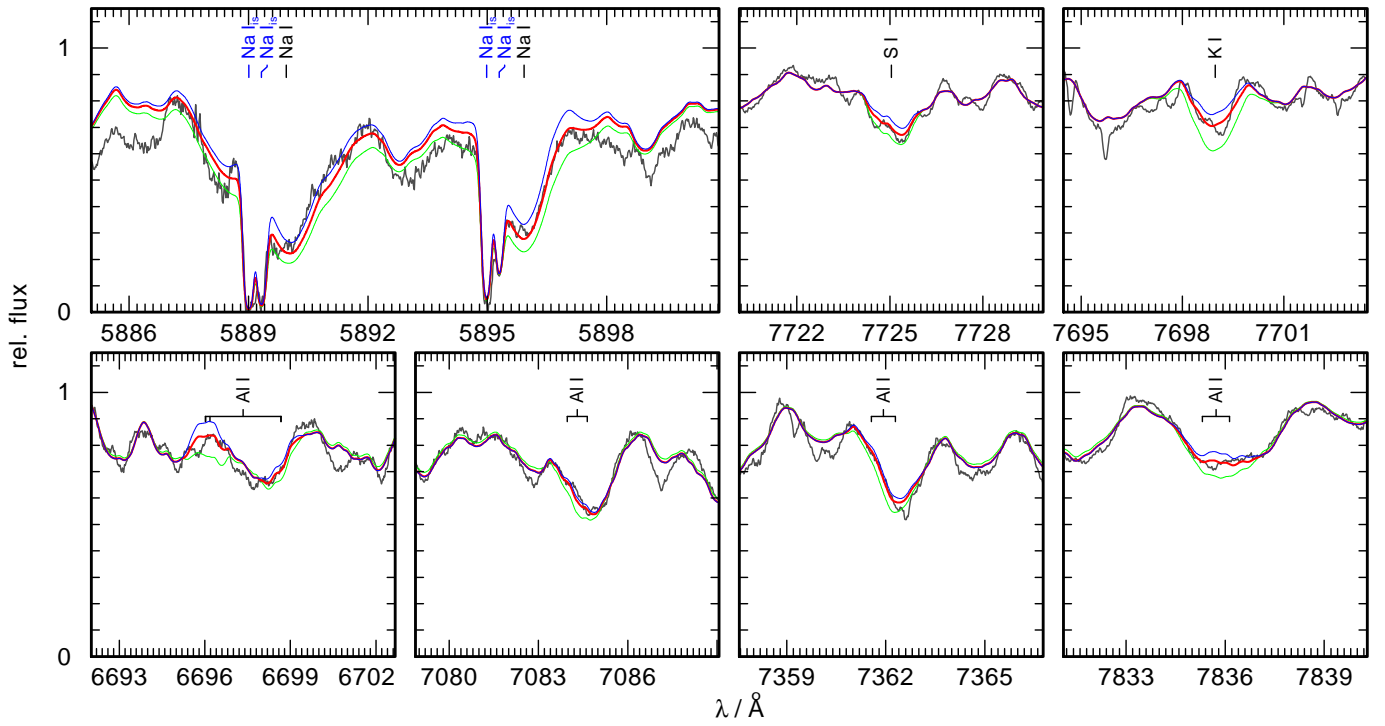


Fig. A.4: Observation (gray) of Hen2–39 compared to model spectra for selected regions around absorption lines of Na I for $[\text{Na}/\text{Fe}] = 0.35, 0.05, -0.25$ (green, red, and blue, respectively), S I for $[\text{S}/\text{Fe}] = 2.17, 1.17, 0.17$, Al I for $[\text{Al}/\text{Fe}] = 0.68, -0.32, -1.32$, and K I for $[\text{K}/\text{Fe}] = 1.07, 0.07, -0.93$. Interstellar absorption lines are indicated with blue marks.

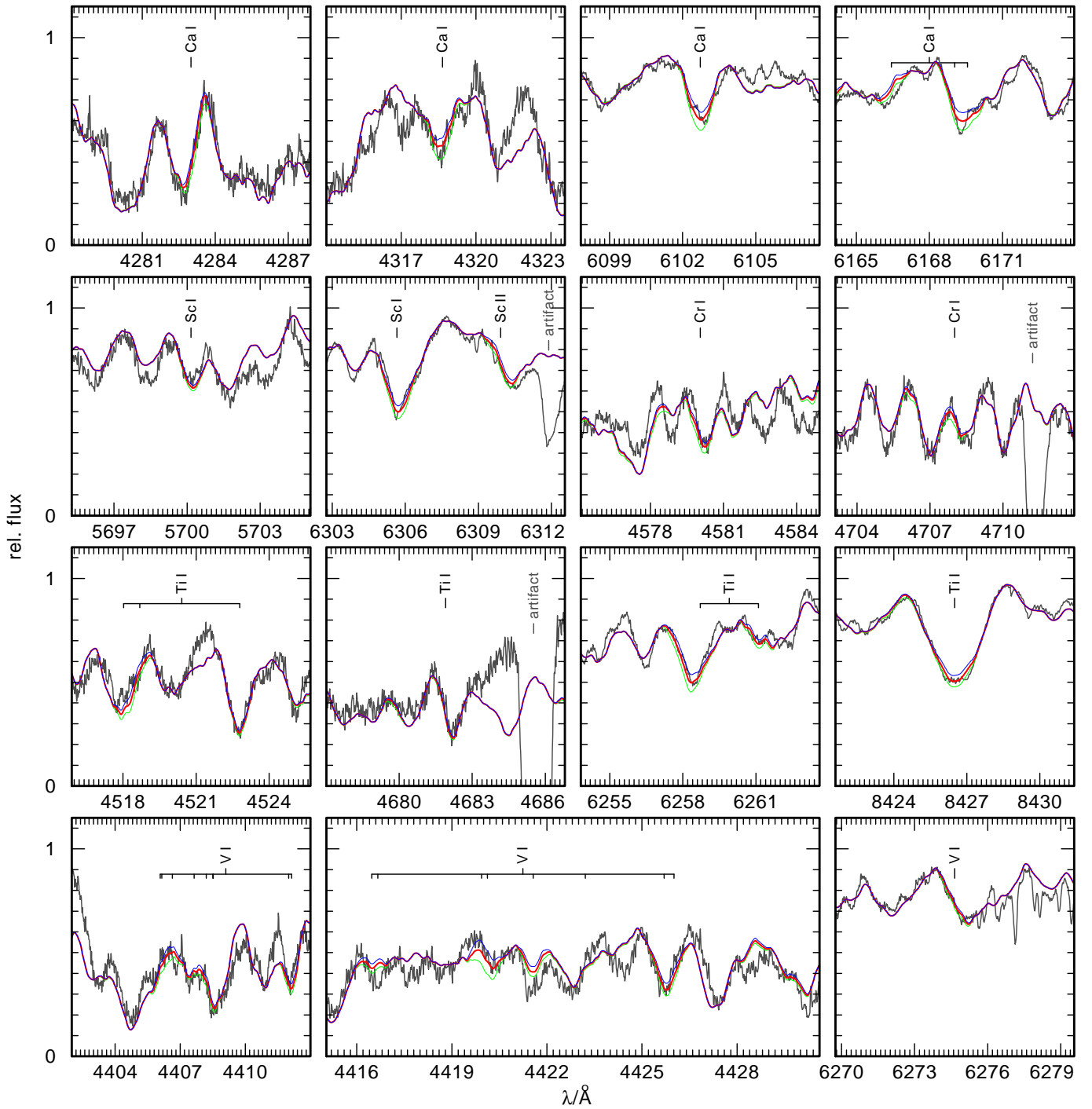


Fig. A.5: Observation (gray) of Hen 2–39 compared to model spectra for selected regions around absorption lines of Ca I for $[\text{Ca}/\text{Fe}] = 0.41, -0.09, -0.59$ (green, red, and blue, respectively), Sc I for $[\text{Sc}/\text{Fe}] = 0.08, -0.42, -0.92$, Cr I for $[\text{Cr}/\text{Fe}] = 0.32, -0.18, -0.68$, Ti I for $[\text{Ti}/\text{Fe}] = -0.13, -0.63, -1.13$, and V I for $[\text{V}/\text{Fe}] = -0.05, -0.55, -1.05$. Artifacts arising from the overcorrection of nebula lines are indicated.

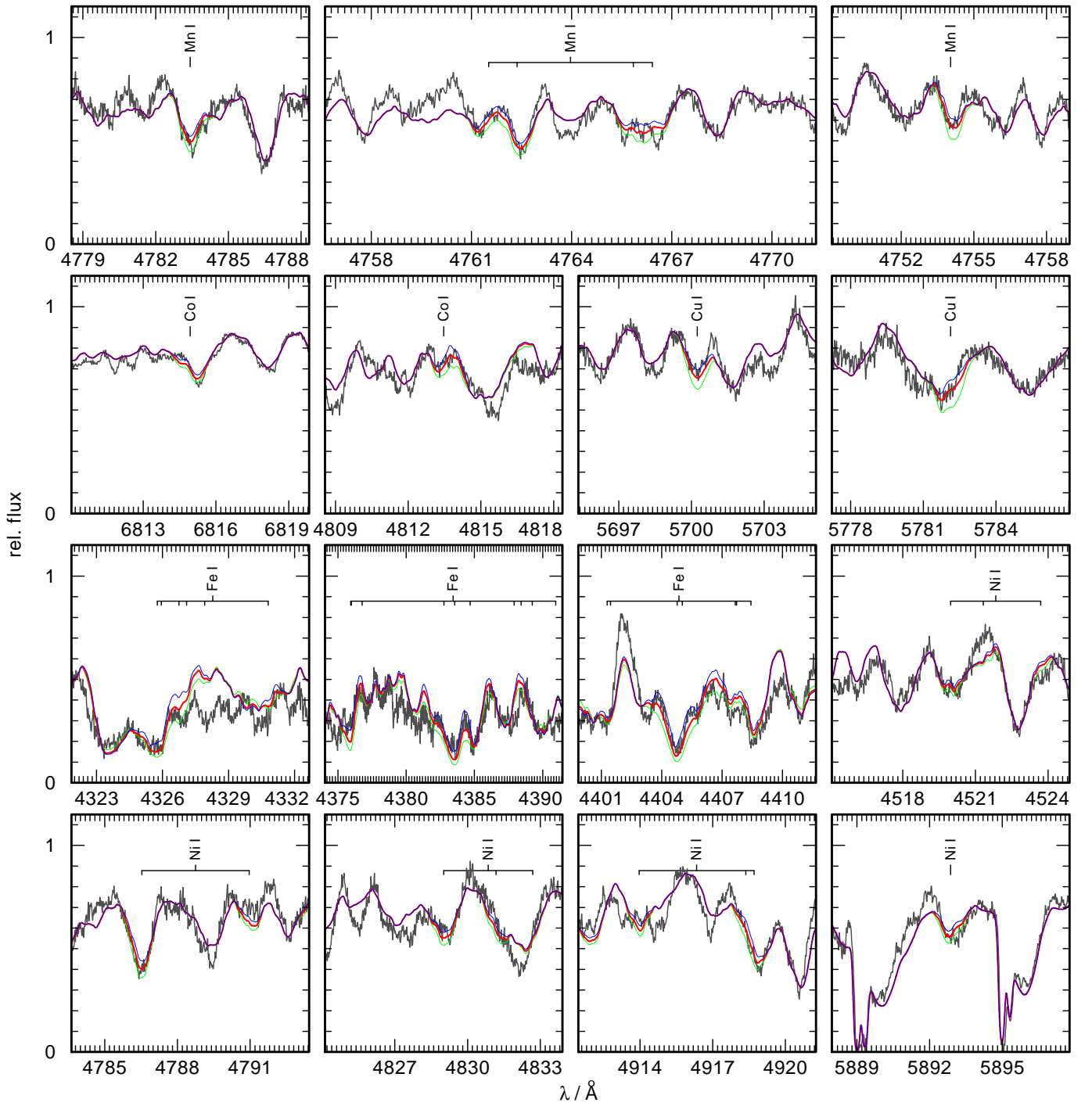


Fig. A.6: Observation (gray) of Hen 2–39 compared to model spectra for selected regions around absorption lines of Mn I for $[\text{Mn}/\text{Fe}] = 0.52, 0.02, -0.48$ (green, red, and blue, respectively), Co I for $[\text{Co}/\text{Fe}] = 1.03, 0.53, 0.03$, Cu I for $[\text{Cu}/\text{Fe}] = 2.18, 1.18, 0.18$, Fe I for $[\text{Fe}/\text{H}] = 0.15, -0.35, -0.85$, and Ni I for $[\text{Ni}/\text{Fe}] = 1.09, 0.59, 0.09$. Interstellar absorption lines are indicated with blue marks.

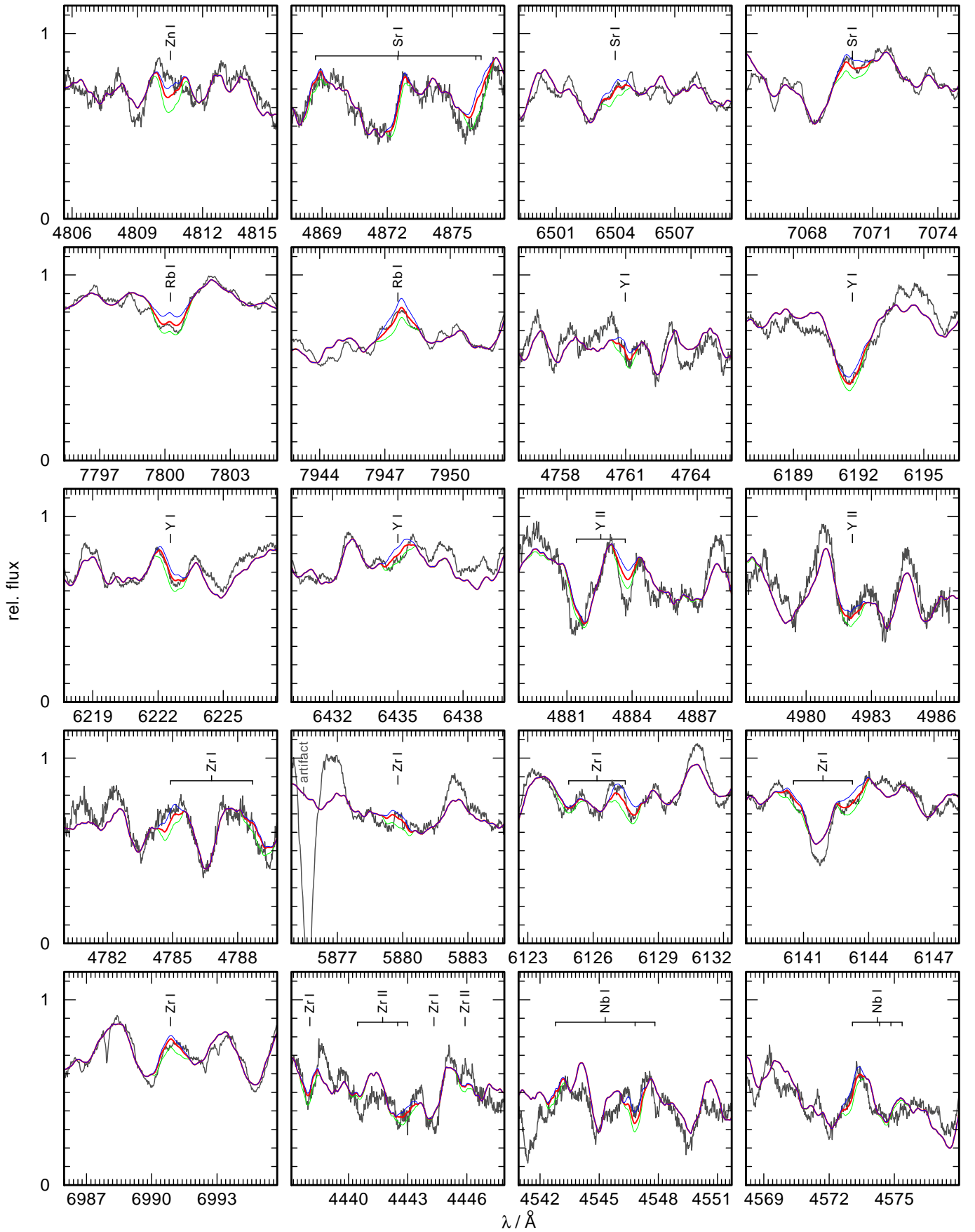


Fig. A.7: Observation (gray) of Hen 2–39 compared to model spectra for selected regions around absorption lines of Zn I for $[\text{Zn}/\text{Fe}] = 2.51, 1.51, 0.51$ (green, red, and blue, respectively), Sr I for $[\text{Sr}/\text{Fe}] = 1.99, 0.99, -0.01$, Rb I for $[\text{Rb}/\text{Fe}] = 2.41, 1.41, 0.41$, Y I and Y II for $[\text{Y}/\text{Fe}] = 1.37, 0.37, -0.63$, Zr I and Zr II for $[\text{Zr}/\text{Fe}] = 1.19, 0.19 - 0.81$, and Nb I for $[\text{Nb}/\text{Fe}] = 1.97, 0.97, -0.03$. Artifacts arising from the overcorrection of nebula lines are indicated.

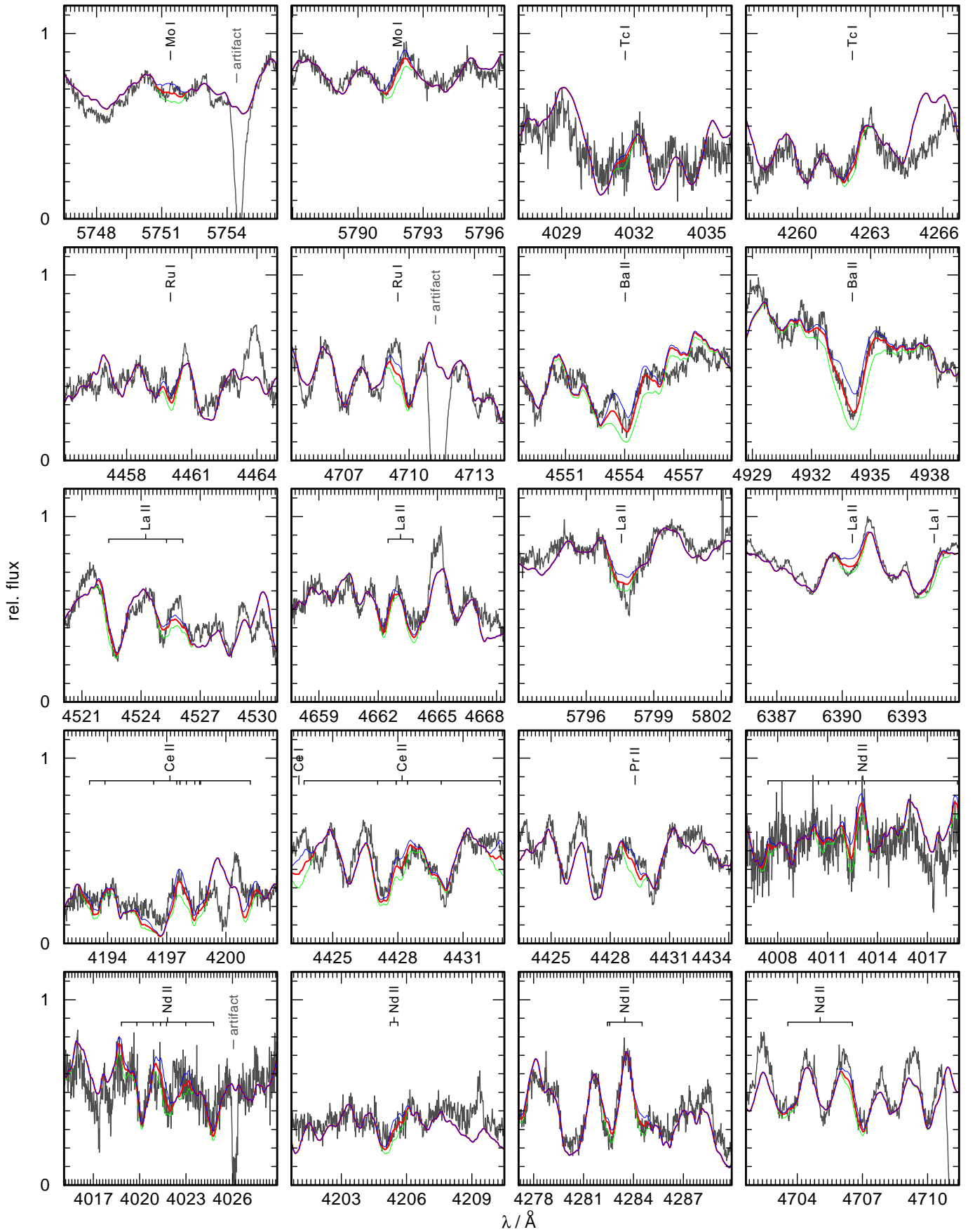


Fig. A.8: Observation (gray) of Hen 2–39 compared to model spectra for selected regions around absorption lines of Mo I for $[\text{Mo}/\text{Fe}] = 2.35, 1.35, 0.35$ (green, red, and blue, respectively), Tc I for $\log \epsilon_{\text{Tc}} = 3.5, 2.5, 1.5$, Ru I for $[\text{Ru}/\text{Fe}] = 3.05, 2.05, 1.05$, Ba II $[\text{Ba}/\text{Fe}] = 2.29, 1.79, 1.27$, La II for $[\text{La}/\text{Fe}] = 2.44, 1.44, 0.44$, Ce I and Ce II for $[\text{Ce}/\text{Fe}] = 3.29, 2.29, 1.29$, Pr II for $[\text{Pr}/\text{Fe}] = 3.68, 2.68, 1.68$, and Nd I for $[\text{Nd}/\text{Fe}] = 1.76, 0.76, -0.24$. Artifacts arising from the overcorrection of nebula lines are indicated.

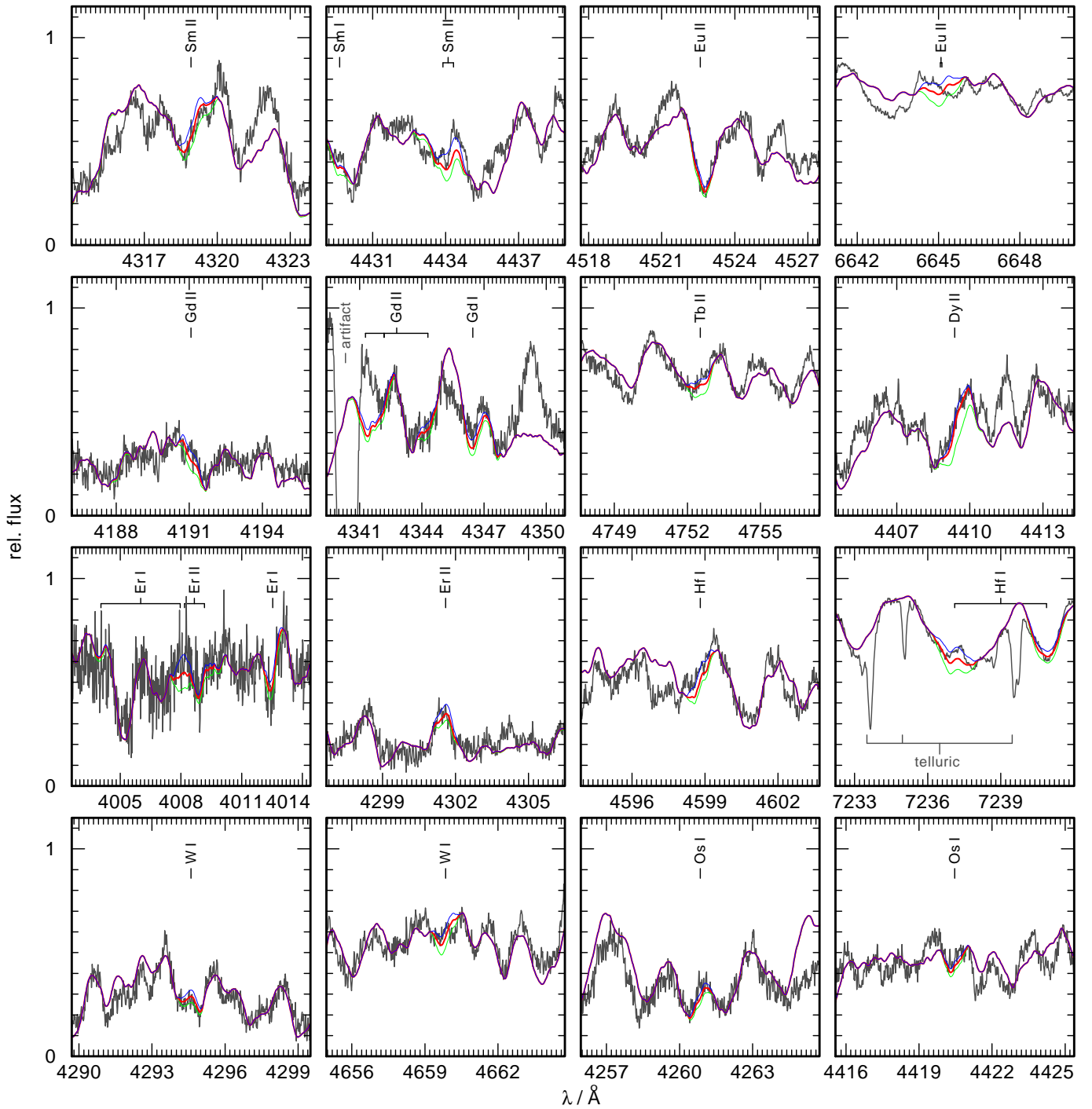


Fig. A.9: Observation (gray) of Hen 2–39 compared to model spectra for selected regions around absorption lines of Sm I and Sm II for $[\text{Sm}/\text{Fe}] = 2.08, 1.08, 0.08$ (green, red, and blue, respectively), Eu II for $[\text{Eu}/\text{Fe}] = 1.95, 0.95, -0.05$, Gd I and Gd II $[\text{Gd}/\text{Fe}] = 2.80, 1.80, 0.80$, Tb II for $[\text{Tb}/\text{Fe}] = 1.79, 0.79, -0.21$, Dy II for $[\text{Dy}/\text{Fe}] = 4.75, 3.75, 2.75$, Er I and Er II $[\text{Er}/\text{Fe}] = 2.86, 1.86, 0.86$, Hf I for $[\text{Hf}/\text{Fe}] = 2.31, 1.31, 0.31$, W I for $[\text{W}/\text{Fe}] = 2.05, 1.05, 0.05$, and Os I for $[\text{Os}/\text{Fe}] = 2.76, 1.76, 0.76$. Artifacts arising from the overcorrection of nebula lines are indicated.

Table A.2: Diagnostic lines used for the determination of stellar parameters. If no interval is given, the line belongs to the previous interval.

λ interval / \AA	λ_{line} / \AA	Ion	E_{low} / cm^{-1}	E_{up} / cm^{-1}	$\log gf$
4020.400 \pm 1.30	4020.400	Sc I	0	24866	-0.130
4023.690 \pm 1.30	4023.690	Sc I	168	25014	0.210
4045.820 \pm 1.30	4045.820	Fe I	11976	36686	0.280
4054.544 \pm 1.30	4054.544	Sc I	0	24657	-0.750
4063.605 \pm 1.30	4063.605	Fe I	12561	37163	0.072
4071.740 \pm 1.30	4071.740	Fe I	12969	37521	-0.022
4082.390 \pm 1.30	4082.390	Sc I	168	24657	-0.444
4233.170 \pm 1.30	4233.170	Fe II	20831	44447	-1.995
4271.760 \pm 1.30	4271.760	Fe I	11976	35379	-0.164
4305.820 \pm 1.40	4305.720	Sc II	4803	28021	-1.200
	4305.910	Ti I	6843	30060	0.300
4307.900 \pm 1.30	4307.900	Fe I	12561	35768	-0.300
4314.080 \pm 1.30	4314.080	Sc II	4988	28161	-0.220
4320.750 \pm 1.30	4320.750	Sc II	4883	28021	-0.100
4325.010 \pm 1.30	4325.010	Sc II	4803	27918	-0.250
4325.760 \pm 1.30	4325.760	Fe I	12969	36079	-0.300
4351.769 \pm 1.30	4351.769	Fe II	21812	44785	-2.100
4374.472 \pm 1.30	4374.472	Sc II	4988	27841	-0.640
4383.550 \pm 1.30	4383.550	Fe I	11976	34782	0.200
4395.040 \pm 1.30	4395.040	Ti II	8744	31491	-0.660
4400.398 \pm 1.30	4400.398	Sc II	4883	27602	-0.480
4404.761 \pm 1.30	4404.761	Fe I	12561	35257	-0.142
4415.560 \pm 1.30	4415.560	Sc II	4803	27444	-0.510
4443.812 \pm 1.30	4443.812	Ti II	8710	31207	-0.690
4468.500 \pm 1.30	4468.500	Ti II	9118	31491	-0.270
4501.273 \pm 1.30	4501.273	Ti II	8998	31207	-0.684
4522.634 \pm 1.30	4522.634	Fe II	22939	45044	-2.119
4534.400 \pm 2.50	4533.239	Ti I	6843	28896	0.563
	4533.969	Ti II	9976	32025	-0.612
	4534.778	Ti I	6743	28788	0.376
	4535.570	Ti I	6661	28703	0.172
4549.550 \pm 1.45	4549.474	Fe II	22810	44785	-1.957
	4549.617	Ti II	12775	34748	-0.110
4555.893 \pm 1.30	4555.893	Fe II	22810	44754	-2.281
4563.761 \pm 1.30	4563.761	Ti II	9851	31757	-0.795
4571.968 \pm 1.30	4571.968	Ti II	12677	34543	-0.209
4629.339 \pm 1.30	4629.339	Fe II	22637	44233	-2.379
4670.407 \pm 1.30	4670.407	Sc II	10945	32350	-0.518
4920.000 \pm 5.00	4915.233	Ti I	15220	35560	-0.945
	4918.954	Fe I	33507	53831	-0.672
	4918.993	Fe I	23111	43435	-0.365
	4919.867	Ti I	17424	37744	-0.260
	4920.502	Fe I	22846	43163	0.058
	4921.769	Ti I	17540	37852	-0.005
	4922.827	Sc I	16023	36331	-0.418
	4923.927	Fe II	23318	43621	-1.319
4981.732 \pm 1.30	4981.732	Ti I	6843	26911	0.586
5701.545 \pm 1.00	5701.545	Fe I	20641	38175	-1.565
5705.464 \pm 1.00	5705.466	Fe I	34692	52214	-1.581
5732.000 \pm 1.30	5731.762	Fe I	34329	51771	-1.174
	5732.275	Fe I	40257	57698	-1.191
5747.954 \pm 1.00	5747.954	Fe I	37163	54555	-0.599
5861.108 \pm 1.00	5861.107	Fe I	34547	51604	-2.761
5934.654 \pm 1.00	5934.653	Fe I	31686	48532	-1.192
5952.800 \pm 1.00	5952.716	Fe I	32134	48928	-2.513
	5952.889	Fe I	34040	50833	-3.725
6151.617 \pm 1.00	6151.617	Fe I	17550	33802	-3.582
6165.360 \pm 1.00	6165.361	Fe I	33413	49628	-1.667

Table A.2: Continued.

λ interval / Å	λ_{line} / Å	Ion	E_{low} / cm ⁻¹	E_{up} / cm ⁻¹	log gf
6170.500 ± 1.00	6170.504	Fe I	38678	54880	-0.654
	6171.006	Fe I	38175	54376	-1.788
6173.334 ± 1.00	6173.341	Fe I	17927	34122	-3.081
	6173.642	Fe I	35856	52050	-3.413
6191.500 ± 1.00	6191.558	Fe I	19621	35768	-1.287
6210.658 ± 1.30	6210.658	Sc I	0	16097	-1.090
6265.132 ± 1.00	6265.141	Fe I	17550	33507	-2.834
6305.657 ± 1.30	6305.657	Sc I	168	16023	-0.950
6318.000 ± 1.00	6318.018	Fe I	19788	35612	-2.338
6336.823 ± 1.00	6336.830	Fe I	29733	45509	-1.260
6408.000 ± 1.00	6407.643	Fe I	32874	48476	-3.620
	6408.026	Fe I	29733	45334	-1.230
	6408.332	Fe I	35379	50980	-3.563
6475.624 ± 1.00	6475.632	Fe I	20641	36079	-3.070
6481.870 ± 1.00	6481.878	Fe I	18378	33802	-3.080
6807.000 ± 1.00	6806.622	Fe I	44023	58710	-1.744
	6806.843	Fe I	21999	36686	-3.210
	6807.288	Fe I	42533	57219	-2.735
6810.262 ± 1.00	6810.262	Fe I	37158	51837	-1.120
8434.957 ± 1.30	8434.957	Ti I	6843	18695	-0.886
8514.400 ± 1.90	8514.072	Fe I	17727	29469	-2.229
	8515.109	Fe I	24339	36079	-2.073
8518.300 ± 1.50	8518.028	Ti I	17215	28952	-1.250
	8518.352	Ti I	15157	26893	-1.089
8582.350 ± 1.35	8582.258	Fe I	24119	35768	-2.133
8611.800 ± 0.90	8611.803	Fe I	22947	34556	-1.900
8679.000 ± 2.10	8678.997	Fe I	48516	60035	-3.806
	8679.632	Fe I	40052	51570	-1.512
8682.900 ± 1.30	8682.979	Ti I	8492	20006	-1.941
8688.950 ± 1.65	8688.624	Fe I	17550	29056	-1.212
8692.000 ± 1.00	8692.331	Ti I	8437	19938	-2.295
8711.500 ± 3.00	8710.174	Mg I	47841	59319	-1.550
	8710.392	Fe I	39626	51103	-0.555
	8712.676	Mg I	47844	59319	-1.670
	8713.188	Fe I	23784	35257	-3.148
8730.750 ± 0.95	8730.497	Ti I	27026	38477	-2.024
8735.250 ± 1.75	8734.712	Ti I	8492	19938	-2.384
	8736.020	Mg I	47957	59401	-0.690
8742.250 ± 0.75	8742.446	Si I	47352	58787	-0.630
8757.200 ± 1.60	8757.187	Fe I	22947	34363	-2.026
8792.850 ± 1.35	8793.342	Fe I	37163	48532	-0.196
8806.000 ± 2.70	8806.756	Mg I	35051	46403	-0.137
	8808.170	Fe I	40405	51754	-1.109
8824.360 ± 1.15	8824.220	Fe I	17727	29056	-1.540
8838.750 ± 1.25	8838.428	Fe I	23052	34363	-1.980

Table A.3: Diagnostic lines used for our determination of element abundances.

λ_{line} / Å	Ion	E_{low} / cm ⁻¹	E_{up} / cm ⁻¹	log gf
5889.951	Na I	0	16973	0.101
5895.924	Na I	0	16956	-0.197
6696.185	Al I	32435	47365	-1.576
6698.670	Al I	25438	40272	-1.960
6698.673	Al I	25348	40272	-1.647
6905.646	Al I	32435	46912	-1.287
7083.969	Al I	32435	46548	-1.111
7361.568	Al I	32435	46016	-0.903
7835.309	Al I	32435	45195	-0.649
7836.134	Al I	32437	45195	-0.494

Table A.3: continued.

$\lambda_{\text{line}} / \text{\AA}$	Ion	$E_{\text{low}} / \text{cm}^{-1}$	$E_{\text{up}} / \text{cm}^{-1}$	$\log g_f$
7836.134	Al I	32437	45195	-1.795
8773.896	Al I	32437	43831	-0.161
8773.898	Al I	32437	43831	-1.462
7725.046	S I	9239	22180	-6.000
7698.974	K I	0	12985	-0.170
5857.451	Ca I	23652	40720	0.257
6161.297	Ca I	20349	36575	-1.293
6162.173	Ca I	15316	31539	-0.167
6169.042	Ca I	20349	36555	-0.804
6169.563	Ca I	20371	36575	-0.527
6343.308	Ca I	35819	51579	0.845
6361.786	Ca I	35897	51611	0.954
6449.810	Ca I	20335	35835	-0.550
6455.600	Ca I	20349	35835	-1.350
6462.570	Ca I	20349	35819	0.310
6471.668	Ca I	20371	35819	-0.680
6493.788	Ca I	20335	35730	0.140
6499.654	Ca I	20349	35730	-0.650
8498.023	Ca II	13650	25414	-1.312
8542.091	Ca II	13711	25414	-0.362
8662.141	Ca II	13650	25192	-0.623
4729.200	Sc I	11520	32659	-0.502
4729.236	Sc I	11558	32697	-0.385
4734.105	Sc I	11520	32637	-0.110
4753.161	Sc I	0	21033	-1.658
4779.348	Sc I	168	21086	-1.613
4791.511	Sc I	168	21033	-2.075
5700.164	Sc I	11558	29096	0.290
5717.307	Sc I	11610	29096	-0.505
5724.107	Sc I	11558	29023	-0.627
6305.657	Sc I	168	16023	-0.950
6378.807	Sc I	0	15673	-2.632
6413.324	Sc I	168	15757	-2.677
4314.080	Sc II	4988	28161	-0.220
4431.370	Sc II	4883	27444	-1.830
6279.740	Sc II	12102	28021	-1.265
6309.920	Sc II	12074	27918	-1.630
4455.320	Ti I	11640	34079	0.480
4518.023	Ti I	6661	28788	-0.252
4522.796	Ti I	6599	28703	-0.265
4533.239	Ti I	6843	28896	0.563
4534.778	Ti I	6743	28788	0.376
4535.570	Ti I	6661	28703	0.172
4535.916	Ti I	6599	28639	-0.026
4536.043	Ti I	6557	28596	-0.129
4548.765	Ti I	6661	28639	-0.274
4552.456	Ti I	6743	28703	-0.262
4656.468	Ti I	0	21469	-1.344
4681.908	Ti I	387	21740	-1.129
4981.732	Ti I	6843	26911	0.586
6258.713	Ti I	11777	27750	-0.090
8382.530	Ti I	6599	18525	-1.632
8426.506	Ti I	6661	18525	-1.253
4025.140	Ti II	4898	29734	-1.960
4394.060	Ti II	9851	32603	-1.669
4395.040	Ti II	8744	31491	-0.660
4417.720	Ti II	9396	32026	-1.240
4468.500	Ti II	9118	31491	-0.270
4549.617	Ti II	12775	34748	-0.110
4563.761	Ti II	9851	31757	-0.795

Table A.3: continued.

$\lambda_{\text{line}} / \text{\AA}$	Ion	$E_{\text{low}} / \text{cm}^{-1}$	$E_{\text{up}} / \text{cm}^{-1}$	$\log gf$
4352.870	V I	553	23520	-0.800
4379.240	V I	2425	25254	0.600
4384.706	V I	553	23353	-1.905
4384.720	V I	2311	25112	0.000
4395.230	V I	2153	24899	0.320
4406.072	V I	8579	31268	-1.000
4406.640	V I	2425	25112	-0.280
4407.637	V I	2311	24993	-0.840
4408.200	V I	2220	24899	-0.100
4408.508	V I	2112	24789	-0.610
4408.512	V I	2153	24830	-0.130
4408.520	V I	2112	24789	-0.820
4419.940	V I	2220	24839	-1.480
4420.120	V I	2153	24771	-2.252
4459.760	V I	2311	24728	-0.570
4460.290	V I	2425	24839	-0.240
5698.520	V I	8579	26122	-0.036
5727.048	V I	8716	26172	0.088
5737.059	V I	8579	26004	-0.675
6135.361	V I	8476	24771	-0.750
6150.157	V I	2425	18680	-1.277
6243.105	V I	2425	18438	-0.878
6274.649	V I	2153	18086	-1.657
6531.440	V I	9825	25131	-1.320
6531.466	V I	23935	39241	-2.931
4274.800	Cr I	0	23386	-0.231
4274.891	Cr I	24200	47586	-2.233
4289.720	Cr I	0	23305	-0.360
4527.332	Cr I	20524	42606	-0.906
4535.695	Cr I	20524	42565	-0.570
4600.741	Cr I	8095	29825	-1.305
4600.775	Cr I	23934	45663	-2.354
4652.152	Cr I	8095	29585	-1.026
4708.018	Cr I	25549	46783	0.110
4718.426	Cr I	25771	46959	0.097
4829.314	Cr I	20524	41225	-1.630
4829.372	Cr I	20524	41225	-0.787
5783.886	Cr I	26796	44081	-0.177
5787.965	Cr I	26796	44069	0.033
5791.006	Cr I	26788	44051	0.324
6924.179	Cr I	27820	42258	-0.135
7462.378	Cr I	23499	36896	-0.040
8947.180	Cr I	25039	36212	-0.724
4554.988	Cr II	32837	54784	-1.249
4235.295	Mn I	23297	46901	-0.030
4458.260	Mn I	24788	47212	-0.042
4761.512	Mn I	23819	44815	-0.138
4762.367	Mn I	23297	44289	0.426
4765.846	Mn I	23720	44696	-0.077
4766.418	Mn I	23549	44523	0.098
4823.524	Mn I	18705	39431	0.144
6013.513	Mn I	24779	41404	-0.397
4045.820	Fe I	11976	36686	0.280
4063.605	Fe I	12561	37163	0.072
4063.627	Fe I	33096	57698	-0.691
4071.740	Fe I	12969	37521	-0.022
4271.760	Fe I	11976	35379	-0.164
4325.739	Fe I	0	23111	-4.815
4325.760	Fe I	12969	36079	-0.300
4383.550	Fe I	11976	34782	0.200

Table A.3: continued.

$\lambda_{\text{line}} / \text{\AA}$	Ion	$E_{\text{low}} / \text{cm}^{-1}$	$E_{\text{up}} / \text{cm}^{-1}$	$\log gf$
4404.761	Fe I	12561	35257	-0.142
5701.545	Fe I	20641	38175	-1.565
4233.113	Fe II	54871	78487	-3.448
4233.137	Fe II	74498	98115	-2.864
4233.170	Fe II	20831	44447	-1.995
4555.893	Fe II	22810	44754	-2.281
4813.449	Co I	23153	43922	-2.121
4813.467	Co I	25938	46707	0.050
6450.247	Co I	13796	29295	-1.698
6814.942	Co I	15774	30444	-1.700
7052.868	Co I	15774	29949	-1.440
4519.979	Ni I	13521	35639	-2.570
4715.757	Ni I	28578	49778	-0.331
4786.531	Ni I	27580	48467	-0.244
4831.169	Ni I	29084	49778	-0.291
4918.362	Ni I	30980	51306	-0.109
4984.112	Ni I	30619	50678	0.226
5892.868	Ni I	16017	32982	-2.141
6314.653	Ni I	15610	31442	-2.402
6482.810	Ni I	15610	31031	-2.630
6914.559	Ni I	15734	30192	-2.270
7409.346	Ni I	30619	44112	-0.237
7414.500	Ni I	16017	29501	-2.570
5700.237	Cu I	13245	30784	-2.312
5782.127	Cu I	13245	30535	-1.720
4810.528	Zn I	32890	53672	-0.137
7800.259	Rb I	0	12817	0.137
7947.597	Rb I	0	12579	-0.167
4741.918	Sr I	14318	35400	-0.320
4872.488	Sr I	14504	35022	-0.200
6504.000	Sr I	18067	33442	0.260
7070.070	Sr I	14899	29039	-0.180
4235.934	Y I	530	24131	-0.490
4839.855	Y I	11532	32188	0.480
6191.718	Y I	0	16146	-0.970
6222.578	Y I	0	16066	-1.700
6435.004	Y I	530	16066	-0.820
4235.730	Y II	1045	24647	-1.425
4982.129	Y II	8328	28394	-1.290
7881.881	Y II	14833	27517	-0.570
4236.550	Zr I	0	23604	-1.000
4772.323	Zr I	5023	25972	0.040
4784.913	Zr I	5540	26434	-0.490
5879.782	Zr I	1241	18244	-1.670
6127.475	Zr I	1241	17556	-1.060
6134.585	Zr I	0	16296	-1.280
6143.252	Zr I	570	16844	-1.100
6990.869	Zr I	5023	19324	-1.220
7102.954	Zr I	5249	19324	-0.840
8070.115	Zr I	5889	18277	-0.790
4443.000	Zr II	11984	34485	-0.160
4205.303	Nb I	392	24165	-0.850
4523.397	Nb I	1143	23244	-0.800
4546.818	Nb I	1587	23574	-0.750
4573.075	Nb I	2154	24015	-0.560
4663.818	Nb I	1587	23023	-0.740
5751.408	Mo I	11454	28837	-1.014
5791.839	Mo I	11454	28715	-1.046
5858.266	Mo I	11858	28924	-0.996
6619.134	Mo I	10768	25872	-1.252

Table A.3: continued.

$\lambda_{\text{line}} / \text{\AA}$	Ion	$E_{\text{low}} / \text{cm}^{-1}$	$E_{\text{up}} / \text{cm}^{-1}$	$\log gf$
4031.626	Tc I	2573	27370	0.39
4095.668	Tc I	3251	27660	-0.01
4238.191	Tc I	0	23588	-0.39
4262.270	Tc I	0	23455	-0.18
4297.058	Tc I	0	23265	-0.03
4206.015	Ru I	8084	31853	-0.480
4385.385	Ru I	7483	30280	-0.610
4385.645	Ru I	9058	31853	-0.490
4410.025	Ru I	9184	31853	-0.380
4460.027	Ru I	8771	31186	-0.530
4554.517	Ru I	6545	28495	0.130
4554.029	Ba II	0	21952	0.170
4934.076	Ba II	0	20262	-0.150
5853.668	Ba II	4874	21952	-1.000
6141.713	Ba II	5675	21952	-0.076
6496.930	Ba II	4874	20262	0.130
4354.400	La II	7340	30305	-0.210
4354.412	La II	7395	30353	-0.500
4526.111	La II	6227	28315	-0.770
4574.860	La II	1394	23247	-1.140
4662.498	La II	0	21442	-1.240
4970.386	La II	2592	22705	-1.190
5797.565	La II	1971	19214	-1.410
5805.773	La II	1016	18236	-1.610
6390.477	La II	2592	18236	-1.450
4324.785	Ce II	7713	30829	-0.514
4324.790	Ce II	7662	30785	-0.050
4386.827	Ce II	1874	24663	-0.582
4408.851	Ce II	7234	29909	-0.965
4408.870	Ce II	7179	29860	0.120
4408.894	Ce II	10314	32989	-0.857
4418.780	Ce II	6968	29592	0.310
4427.916	Ce II	4323	26900	-0.460
4427.920	Ce II	4275	26859	-0.610
4427.916	Ce II	4323	26900	-0.460
4427.920	Ce II	4275	26859	-0.610
4428.438	Ce II	4266	26841	-0.657
4444.700	Ce II	8532	31024	0.110
4483.893	Ce II	6968	29263	0.010
4483.900	Ce II	6937	29239	-0.050
4572.278	Ce II	5514	27378	0.001
4429.254	Pr II	2998	25569	-0.010
4205.600	Nd II	5086	28857	0.070
4232.380	Nd II	513	24134	-1.020
4351.290	Nd II	1470	24445	-1.210
4358.161	Nd II	2585	25524	-0.280
4358.170	Nd II	4512	27449	-0.060
4358.161	Nd II	2585	25524	-0.280
4358.170	Nd II	4512	27449	-0.060
4385.660	Nd II	1650	24445	-0.550
4391.100	Nd II	2585	25352	-0.240
4414.440	Nd II	513	23160	-0.840
4446.390	Nd II	1650	24134	-0.500
4680.737	Nd II	513	21872	-1.260
4706.543	Nd II	0	21241	-0.880
4715.586	Nd II	1650	22850	-1.070
4820.339	Nd II	1650	22390	-1.240
4229.713	Sm II	327	23962	-1.224
4390.855	Sm II	1489	24257	-0.804
4420.524	Sm II	2689	25304	-0.695

Table A.3: continued.

$\lambda_{\text{line}} / \text{\AA}$	Ion	$E_{\text{low}} / \text{cm}^{-1}$	$E_{\text{up}} / \text{cm}^{-1}$	$\log gf$
4433.890	Sm II	3499	26046	-0.572
4676.902	Sm II	327	21702	-1.407
4522.581	Eu II	1669	23774	-0.678
6645.064	Eu II	11128	26173	0.204
7426.569	Eu II	10313	23774	-0.149
4053.640	Gd I	999	25661	0.297
4191.075	Gd II	3444	27298	-0.653
4394.720	Gd II	6533	29288	-0.060
4394.720	Gd II	6605	29353	-1.783
4752.526	Tb II	0	21036	-0.816
4186.819	Dy I	0	23878	0.693
4077.966	Dy II	828	25343	-0.058
4409.383	Dy II	0	22673	-1.420
4301.596	Er II	0	23241	-1.487
4419.608	Er II	13572	36192	0.386
7131.816	Hf I	0	14018	-1.690
7237.112	Hf I	4568	18382	-0.840
4294.605	W I	2951	26230	-0.735
4659.853	W I	0	21454	-1.900
4260.848	Os I	0	23463	-1.440
4420.468	Os I	0	22616	-1.530
4793.993	Os I	4159	25013	-1.990